J. Fluid Mech. (2007), *vol.* 591, *pp.* 215–253. © 2007 Cambridge University Press
doi:10.1017/S0022112007008129 Printed in the United Kingdom

Numerical simulation of the compressible mixing layer past an axisymmetric trailing edge

FRANCK SIMON[1], SEBASTIEN DECK[1],
PHILIPPE GUILLEN[1], PIERRE SAGAUT[2]
AND ALAIN MERLEN[3]

[1]ONERA, Applied Aerodynamics Department, F-92322 Châtillon, France

[2]Institut Jean Le Rond d'Alembert, UMR 7190, Université Pierre et Marie Curie - Paris 6,
F-75005 Paris, France

[3]Laboratoire de Mécanique de Lille, UMR 8107, Université des sciences et technologies de Lille,
F-59655 Villeneuve d'Ascq, France

(Received 23 August 2006 and in revised form 25 June 2007)

Numerical simulation of a compressible mixing layer past an axisymmetric trailing edge is carried out for a Reynolds number based on the diameter of the trailing edge approximately equal to 2.9×10^6. The free-stream Mach number at separation is equal to 2.46, which corresponds to experiments and leads to high levels of compressibility. The present work focuses on the evolution of the turbulence field through extra strain rates and on the unsteady features of the annular shear layer. Both time-averaged and instantaneous data are used to obtain further insight into the dynamics of the flow. An investigation of the time-averaged flow field reveals an important shear-layer growth rate in its initial stage and a strong anisotropy of the turbulent field. The convection velocity of the vortices is found to be somewhat higher than the estimated isentropic value. This corroborates findings on the domination of the supersonic mode in planar supersonic/subsonic mixing layers. The development of the shear layer leads to a rapid decrease of the anisotropy until the onset of streamline realignment with the axis. Due to the increase of the axisymmetric constraints, an adverse pressure gradient originates from the change in streamline curvature. This recompression is found to slow down the eddy convection. The foot shock pattern features several convected shocks emanating from the upper side of the vortices, which merge into a recompression shock in the free stream. Then, the flow accelerates and the compressibility levels quickly drop in the turbulent developing wake. Some evidence of the existence of large-scale structures in the near wake is found through the domination of the azimuthal mode $m = 1$ for a Strouhal number based on trailing-edge diameter equal to 0.26.

1. Introduction

The understanding of free shear flows is of primary interest as they include numerous fundamental but also complex physics features and have been the focus of many studies for decades. As reasonable knowledge of low-speed shear layers was achieved, research interest was pushed toward the supersonic case thus revealing strong differences with subsonic mixing layers. The major discrepancies appear to be a reduction in the shear layer growth rate coupled with a decrease of the turbulent Reynolds stresses magnitude. Such behaviour has been found to be a direct effect of the compressibility and the scaling parameter was found to be the convective Mach number M_c (Bogdanoff 1983; Papamoschou & Roshko 1988). M_c was derived from isentropic assumptions and is

$$M_c = \frac{U_1 - U_2}{a_1 + a_2} \tag{1.1}$$

where the subscripts 1 and 2 respectively describe the high- and the low-speed streams. An early interpretation of this stabilizing effect involved a reduction of communication in the shear layer by Papamoschou (1990) and Breidenthal (1990). First observed in experiments (Papamoschou & Roshko 1988; Papamoschou 1991; Gruber, Messersmith & Dutton 1993; Barre, Quine & Dussauge 1994; Clemens & Mungal 1995) it also has been highlighted by means of direct numerical simulations (DNS) (Sandham & Reynolds 1989; 1991; Sarkar 1995 Vreman, Sandham & Luo 1996 Freund, Lele & Moin 2000; Pantano & Sarkar 2002). It has been demonstrated that the normalized pressure–strain term decreases with increasing M_c. The consequence of this compressibility effect is an energy transfer reduction from the streamwise to cross-stream velocity fluctuations involving a decay of the turbulence production term in the Reynolds stresses transport equation. From a theoretical point of view, such an influence on homogeneous sheared turbulence has also been demonstrated by Simone, Coleman & Cambon (1997) using linear rapid-distortion theory. The use of linear stability analysis of compressible mixing layers gives the same conclusions (Jackson & Grosch 1989; Sandham & Reynolds 1991).

It has been demonstrated that increasing M_c leads to a physical change in the geometry of the large-scale structures. For M_c values less than 0.6, the instability process is bi-dimensional with large spanwise correlated structures originating from the Kelvin–Helmholtz (KH) instability. These spanwise rollers are quite easy to follow in the flow field and phenomena such as pairing or merging can also clearly be observed participating in the shear layer growth. For values above 0.6, oblique waves compete with bi-dimensional instability modes. Finally, when $M_c > 1$, the instability waves are three-dimensional and the growth rate of the most amplified mode is greatly reduced compared to the bi-dimensional mode in low-M_c cases. This shift in the instability process comes with a modification of the coherent-structure shape in supersonic mixing layers. Moreover, these structures are difficult to identify and to track due to their less coherent properties. Pairing and merging processes, seem to be inhibited, at least in the initial stage of development of the free compressible shear layer. Sandham & Reynolds (1991) observed λ-vortices staggered in the streamwise direction at high M_c values. Another important finding of the linear stability studies is the departure from the isentropic M_c model under highly compressible conditions. Jackson & Grosch (1989) have highlighted the existence of a slow mode and a supersonic mode at high M_c in addition to the neutral mode (also called the central mode) already existing in the subsonic case. This explains some experimental observations of asymmetric behaviour of supersonic mixing layers. In the two-stream supersonic–supersonic case, the slow mode develops whereas in the supersonic–subsonic case, the fast mode dominates.

In the case of axisymmetric supersonic shear layers, previous studies (Fourguette, Mungal & Dibble 1991; Freund *et al.* 2000; Thurow, Ssamimy & Lempert 2003) have demonstrated the three-dimensional shape of the turbulent eddies, as in the planar case. Freund (2000) have performed direct simulations of temporally developing round compressible jets in the early stages of their development. They observed a diminution of the velocity fluctuations with the convective Mach number. This behaviour, similar to that encountered in planar shear layers, is somewhat reduced in the axisymmetric case. However, the authors could not state if it was a direct effect of the geometry configuration or due to greater turbulence intensity in the non-similar states of the jet. Moreover, in their more compressible case ($M_c = 0.87$), Thurow *et al.* (2003) observed a bimodal instability with the appearance of both slow and fast modes, which differs from planar mixing layer studies.

However, in some specific cases, axisymmetric compressible shear layers can lead to the occurrence of a wide range of phenomena coupled with complex interactions. To investigate such flows, the separation process past a blunt-base axisymmetric trailing edge is used to generate a supersonic annular shear layer. This particular geometrical configuration involves an important modification of the whole flow field compared to the canonical case. The separating process transforms the incoming boundary layer into an annular mixing layer. On passing through the expansion fan centred at the base, the developing shear layer is deflected toward the axis and then grow on moving downstream. On approaching the axis, concave curvature effects originating from the increasing axisymmetrical constraint appear. An adverse pressure gradient then originates from the change in lateral streamline curvature leading to the formation of a recompression shock in the free stream like that encountered in ramp compression configurations (see for example Adams 2000). On passing through the pressure gradient, the flow realigns with the axis and the axisymmetric mixing layer transitions into a turbulent wake. Both the streamline curvature and the adverse pressure gradient constitute extra strain rates (as defined by Bradshaw (1974) for supersonic boundary layers studies) which can deeply alter the turbulence structure of the flow field.

In the past, due to measurement difficulties, attention has been focused on the far wake. For example, Demetriades (1968, 1976) has experimentally studied the far field behind a slender axisymmetric body and found some evidence of the existence of large-scale structures (organized structures have also been experimentally found in subsonic axisymmetric wakes by Roberts (1973), Fuchs, Mercker & Michel (1979) and more recently by Deprés (2003)). However, excepting the work of Gaviglio *et al.* (1977), the near wake has been studied only very recently thanks to the improvement of non-intrusive measurement tools. Such a case has been experimentally investigated at the University of Illinois where this configuration has received particular attention with the use of visualizations and laser Doppler velocimetry (LDV). A lot of work has been done by Dutton and co-workers in postprocessing instantaneous snapshots to gain insight into the vortex dynamics. However, the experimental nature of their work prevent them from directly acquiring unsteady data in the separated flow field, thus limiting our comprehension of such flows. During the last ten years, several works have been devoted to the simulation of such a flow in order to improve turbulence model predictions or to validate new hybrid numerical approaches (see for example, Fureby, Nilsson & Andersson 1999; Forsythe *et al.* 2002; Baurle *et al.* 2003; Kawai & Fujii 2005). Unfortunately, these numerical studies have focused on time-averaged results and none of them has been used to assess the unsteadiness of the flow, except the study of Sandberg & Fasel (2006*a*, *b*) who investigated the transitional wake at $Re_D = 100\,000$ with D the diameter of the trailing edge, with the use of DNS and linear stability investigations. A major result is the coexistence of convective shear layer instabilities and of an absolute instability of the recirculating flow.

Numerical simulation is therefore a useful tool to go beyond the shortcomings of the available experimental data as some questions remain open:

(i) Does the initial part of the mixing layer behave as in the planar case? What is the dynamics of the eddies in the developing shear layer?

(ii) How do the extra strain rates alter the turbulent field and the shear layer dynamics?

(iii) The far field is known to be self-similar but what happens in the transition region before the wake attains a fully developed state?

(iv) A characteristic feature of such a configuration is the existence of a subsonic recirculating flow enclosed in the supersonic annular mixing layer. What role does this bubble play in the shear layer dynamics and does a forcing through a feedback mechanism exist?

The present work investigates the unsteadiness of the compressible shear layer development past an axisymmetric trailing edge and the influence of extra strain rates on the turbulence field by means of numerical simulation. The paper is organized as follows. First the main features of the experimental setup and the test case will be described. Then, the numerical code and the simulation methodology as well as the mesh grid will be described. A mean flow analysis will be performed to investigate the classical properties of supersonic base flows. In the two following sections, attention will be focused on the description of the shear layer behaviour in terms of time-averaged characteristics, coherent-structure dynamics and spectral analysis. Once the shear layer has been investigated, the recompression region, the turbulent wake development and the recirculation area will be successively considered.

2. Main features of the experimental setup

The supersonic base flow past an axisymmetric trailing edge was experimentally investigated at the University of Illinois Gas Dynamics Laboratory by Herrin & Dutton (1994*a*) for a free-stream Mach number M_∞ equal to 2.46 and a Reynolds number per metre equal to 52×10^6. The wind tunnel was specially designed for axisymmetric base flow investigations and is of blowdown-type. Special care was taken that the axisymmetry of the flow was not altered on the cylinder due to a slight misalignment of the model. This test case has been chosen as a consequence of the great amount of available data to validate the numerical results.

This bluntbase case was investigated using a two-component (LDV) system (Herrin & Dutton (1994*a*, 1995). Conventional schlieren and shadowgraph photography were also used to investigate the coherent-structure properties. Planar flow visualizations (both side and end views) using the single-pulse, planar Mie scattering technique have also been published by Bourdon & Dutton (1999, 2000) and Cannon, Elliott & Dutton (2005). Mean-static pressure measurements and high-frequency measurements using Kulite pressure transducers have been published by Janssen & Dutton (2004).

Also, the planar case (Smith & Dutton 1996; Messersmith & Dutton 1996; Smith & Dutton 1999; 2001) and the boattailed-base case (Herrin & Dutton 1994*b*, 1995, 1997; Bourdon & Dutton 2001) have also received attention, thus providing additional insight into the axisymmetric case.

A detailed description of the wind tunnel facility and of the experimental diagnostics can be found in the above references.

3. Numerical procedure

3.1. *FLU3M code*

The multiblock Navier–Stokes solver used in the present study is the FLU3M code developed by ONERA. The equations are discretized using a second-order- accurate upwind finite volume scheme and a cell-centred discretization. The Euler fluxes are discretized by a modified AUSM+(P) upwind scheme which is fully described in Mary & Sagaut (2002). Time discretization is based on second-order Gear's formulation as presented by Péchier *et al.* (2001). Further details concerning the numerical procedure and the turbulence modelling may be found in Péchier *et al.* (2001) and Deck *et al.* (2002). This numerical strategy has already been applied with success to a wide range of turbulent flows such as the compressible flow over an open cavity at high Reynolds number (Larchevêque *et al.* 2003, 2004) and transonic buffet over a supercritical airfoil (Deck (2005*a*)).

3.2. *Turbulence modelling*

Because of the high Reynolds number of the flow, the methodology used in the present work is the zonal-detached eddy simulation (ZDES) which is derived from the classical detached eddy simulation (called DES97) introduced by Spalart *et al.* (1997). These methodologies are part of the RANS/LES family (for more details, see the discussion by Sagaut, Deck & Terracol 2006).

The model was originally based on the Spalart–Allmaras (SA) model which solves a one-equation turbulence model for the eddy viscosity $\tilde{\nu}$:

$$\frac{D\bar{\rho}\tilde{\nu}}{Dt} = c_{b1}\tilde{S}\bar{\rho}\tilde{\nu} + \frac{1}{\sigma}\left(\frac{\partial}{\partial x_j}(\mu + \bar{\rho}\tilde{\nu})\frac{\partial \tilde{\nu}}{\partial x_j} + c_{b2}\frac{\partial \tilde{\nu}}{\partial x_j}\frac{\bar{\rho}\tilde{\nu}}{\partial x_j}\right) - \bar{\rho}c_{w1}f_w\left(\frac{\tilde{\nu}}{d_w}\right)^2. \tag{3.1}$$

The eddy viscosity is defined as:

$$\mu_t = \rho\tilde{\nu}f_{v1} = \rho\nu_t, \quad f_{v1} = \frac{\chi^3}{\chi^3 + c_{v1}^3}, \quad \chi = \frac{\tilde{\nu}}{\nu}. \tag{3.2}$$

The f_w and f_v functions are near-wall correction functions in the finite-Reynolds-number version of the model and we refer to the original papers Spalart & Allmaras (1992, 1994) for details on the constants and the quantities involved. For the current research, the transition terms of the SA model allowing for a shift from a laminar to a turbulent state were turned off.

What is important here is that the model is provided with a destruction term for the eddy viscosity that contains d, the distance to the closest wall. This term, when balanced with the the production term, adjusts the eddy viscosity to scale with the local deformation rate $\tilde{S}$ producing an eddy viscosity given by:

$$\tilde{\nu} \sim \tilde{S}d^2. \tag{3.3}$$

The idea suggested by Spalart *et al.* (1997) was to modify the destruction term so that the RANS model is reduced to an LES subgrid-scale one in the detached flows. They proposed to replace the distance d to the closest wall with $\tilde{d}$ defined by

$$\tilde{d} = \min(d, C_{DES}\Delta) \tag{3.4}$$

where Δ is a characteristic mesh length. Away from the wall, if the destruction term balances the production one, the eddy viscosity scales with the length Δ and the local vorticity modulus S: $\nu_t \sim S\Delta^2$, then takes the form of Smagorinsky's SGS-viscosity $\nu_{SGS} \sim \sqrt{2S_{ij}S_{ij}}\Delta^2$, where S_{ij} are the components of the strain tensor. Moreover, the subgrid model behaves somewhat like a dynamic model because of the material derivative and the diffusion term. Shur *et al.* (1999) have calibrated the C_{DES} value by performing homogeneous isotropic turbulence simulations using high-order schemes and found a value of 0.65. The use of lower-order spatial schemes suggests lowering this value. In accordance with the previous statement and in agreement with previous work (Simon *et al.* (2006)), the C_{DES} constant was set to 0.55 in the present study.

Originally, we chose to define Δ as the largest of the spacings in all three directions

$$\Delta = \Delta_{max} = \max(\Delta x, \Delta y, \Delta z) \tag{3.5}$$

so that the model 'naturally' switches from the RANS behaviour in the grid region typical of a boundary layer, i.e. $d \ll \Delta = \max(\Delta x, \Delta z)$ ($\boldsymbol{y}$ being normal to the wall) to the LES behaviour away from the wall, i.e. $\Delta \ll d$. Nevertheless, and from the beginning, a special care was given to the region, named the 'grey area', where the model switches, and where the velocity fluctuations (the 'LES content'), are expected to be not sufficiently developed to compensate for the loss of modelled turbulent stresses. This can lead to unphysical outcomes, such as an under-estimation of the skin friction, and so motivated, first, the publication of a paper (Spalart 2001) to specify the character of DES97 meshes, and then, a modification of $\tilde{d}$, presented as a delayed-DES (Spalart *et al.* 2006), to extend the RANS mode and prevent 'modelled-stress depletion'. In order to remove this drawback, Deck (2005*a*, *b*) proposed a zonal approach of the original DES, called zonal-DES or ZDES, in which RANS and DES domains are selected individually. In RANS regions, the model is forced to behave as a RANS model, while in DES regions, the model can switch from the RANS mode to the LES mode by means of (3.4). The zonal approach is well-adapted to treat free shear flows, as the user can focus grid refinements on the regions of interest without corrupting the boundary-layer properties farther upstream or downstream. For instance, in DES regions, the grid is designed to obtain nearly cubic cells. In these regions, Deck also suggested adopting the classical characteristic length scale used in LES and based on the cell volume:

$$\Delta = \Delta_{vol} = (\Delta_x \Delta_y \Delta_z)^{1/3}. \tag{3.6}$$

In addition, the near-wall functions of the RANS model are explicitly disabled in the LES mode of DES regions (but not in the RANS mode) as follows (Breuer, Jovicic & Mazaev 2003):

$$f_{v1} = 1, \quad f_{v2} = 0, \quad f_w = 1. \tag{3.7}$$

This choice avoids the low eddy viscosity levels typical of resolved LES regions being treated as in boundary layers. The use of (3.6) and (3.7) in DES regions justifies its notation being different from DES97. In practice, DES switches very quickly to the LES mode thanks to (3.6) and (3.7). In this way, the LES mode is managed by the transport equation of ν_t calibrated for free shear flows plus a destruction term rescaling the subgrid-scale viscosity as a function of the mesh resolution. To complete the closure of the RANS/SGS stress tensor, its deviatoric part τ^d is linearly linked to the deviatoric part of the resolved strain tensor:

$$\tau_{ij}^d = 2\rho\nu_t(S_{ij} - \tfrac{1}{3}S_{ll}\delta_{ij}) \tag{3.8}$$

while its isotropic part, whose trace equals 2/3 times the specific kinetic energy (of the whole of the turbulence in RANS mode or under the gridscale in LES mode), can be included in the pressure term and is often neglected with respect to it. In the present work, the subgrid kinetic energy is neglected in the total energy equation. This hypothesis is based on the work by Erlebacher *et al.* (1992) who demonstrate that it is reasonable to neglect this term without compromising the flow physics prediction in the case of turbulent Mach numbers M_t lower than 0.60. In the near wake, the turbulent activity leads to M_t levels up to 0.40 when the resolved turbulent

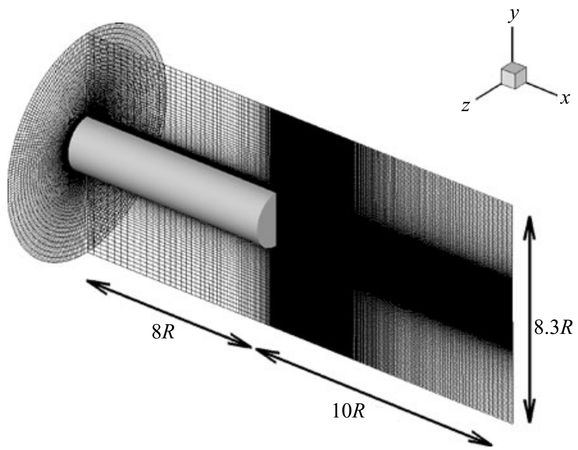

FIGURE 1. The computational mesh.

kinetic energy is considered (see figure 19). As at the same time, the SGS contribution is very weak, this justifies the use of the present numerical model without altering significantly the resolved flow physics.

It has successfully been used to calculate the transonic buffet phenomenon over a supercritical airfoil (Deck 2005*a*) and the flow around a high-lift configuration (Deck 2005*b*). The case of an axisymmetric separating/reattaching shear layer in the subsonic regime has also been assessed recently (Deck & Thorigny 2007). In the supersonic regime, a previous study has successfully examined the present separated base flow (Simon *et al.* 2006).

3.3. *Simulation overview*

The present simulation was performed at a free-stream Mach number M_∞ equal to 2.46 which corresponds to the experimental value. The free-stream velocity U_∞, equal to 593.8 m s^{-1}, gives a Reynolds number Re approximatively equal to 2.9×10^6. The free-stream pressure P_∞ and temperature T_∞ are respectively set to 31415 Pa and 145 K. The base radius R of the trailing edge is equal to 31.75 mm.

The computational mesh used in the present work is plotted in figure 1. The cylinder length is equal to $8R$ in order to fit the experimental boundary layer height δ at separation, while beyond the base, the computational domain extends to $10R$. In addition, the outside boundary is set to $4.15R$ from the axis of symmetry. These dimensions are identical to those used in previous studies such as Forsythe (2002) and Simon (2006). The grid includes nearly 20.7 million cells with 240 cells in the azimuthal direction (1.5 degrees per plan). Behind the base, an O-H topology has been used in order to avoid convergence problems and high CFL values on the axis. Moreover, particular attention has been paid to the cells isotropy in the separated region where the numerical model behaves in the LES mode. An *a posteriori* verification shows that there are at least 15 points in the vorticity thickness in the early stages of its development. On moving downstream, this resolution increases thanks to the mixing-layer growth.

The temporal integration has been performed with four inner Newton sub-iterations and a physical time step equal to 2×10^{-7} s. These choices lead to the decay of at least one order during the convergence process.

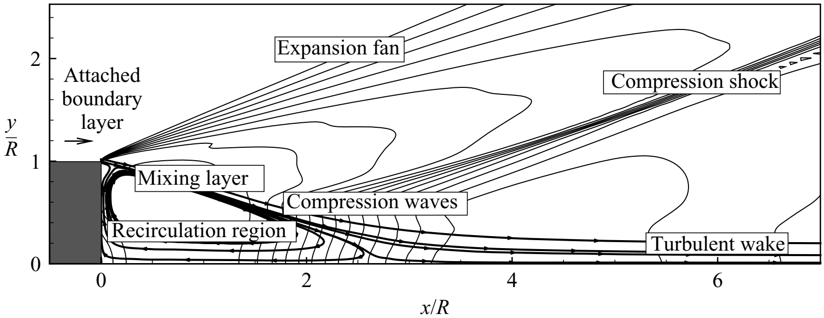

FIGURE 2. Supersonic base flow topology (iso-lines of pressure and computed streamlines).

The averaging process has been performed over a physical time equal to 75 ms which represents slightly less than 80 flow-through times. Based on the estimation of 1 μs per iteration and per grid cell, the simulation cost is equal to approximately 8650 CPU hours on a NEC SX6 processor. In addition to the time-averaged flow field, nearly 430 sensors were also placed in all the relevant areas of the near wake in order to measure the dominant frequencies of the flow. The sampling rate is equal to 250 kHz.

4. Validation

The time-averaged flow field is depicted in figure 2 which highlights the classical topology of the near wake in supersonic blunt-base flows. The incoming turbulent boundary layer separates at the base after passing through an expansion fan shown by the iso-contours of pressure. The free shear flow transforms into a mixing layer exhibiting high compressibility levels. On moving downstream, the mixing process inside the shear layer leads to an equilibrium between the free stream and the low-pressure region behind the trailing edge which represents the recirculating area (also called the ‘dead-air region’ despite its unsteady nature). The streamline curvature in the shear flow then decreases due to the axisymmetric constraint for $1.8 < x/R < 4$. On realigning with the axis, part of the incoming flow has enough momentum to pass through the recompression and to be convected downstream into a turbulent wake. The compression waves coalesce in the free stream and form a recompression shock. The other part of the flow is pushed upstream thus forming a toroidal reverse flow topology. This recirculating region extends to approximately $2.7R$ ($= L_R$) which agrees very well with the experimental value of $2.67R$. The streamline which represents the boundary between the recirculation region and the free stream is called the dividing streamline and its intersection with the axis is named the rear stagnation point.

To validate the present simulation, the shear stress profiles, the main contributor to the turbulence production, are compared to the experimental data in figure 3. The results appear to compare favourably with the LDV data for all the locations considered. The turbulent field is properly predicted, which demonstrates that all the characteristic features of the flow physics are well-captured in the simulation and corroborates the proper prediction of the rear stagnation point location.

As the present work is focused on the unsteady features of the flow, numerical schlieren-like visualizations have been used by plotting iso-contours of $\|\mathrm{grad}(\rho)\|$. Moreover, the existence of coherent structures in the flow field has been assessed with

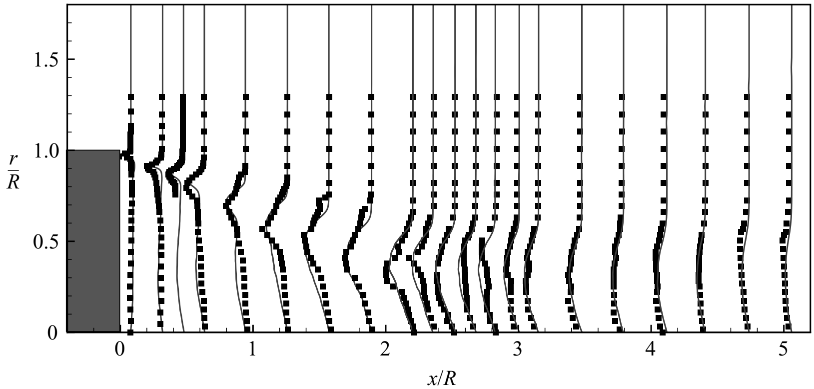

FIGURE 3. Time-averaged shear stress $\overline{u'v'}/U_\infty^2$ profiles (solid line, simulation; ■, experiment).

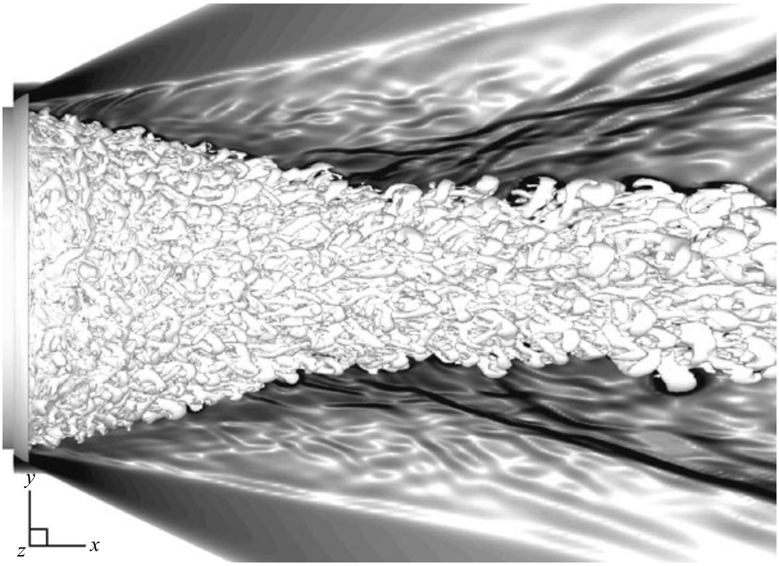

FIGURE 4. Iso-surface of the Q criterion ($Q=(D/U_\infty)^2$) and numerical schlieren-like visualization (iso-contours of $\|\text{grad}(\rho)\|$).

iso-surfaces of the Q criterion (Jeong & Hussain 1995):

$$Q = -\tfrac{1}{2}(\|\boldsymbol{S}\| - \|\boldsymbol{\Omega}\|) \tag{4.1}$$

with $\boldsymbol{S}$ and $\boldsymbol{\Omega}$ denoting respectively the strain and the rotation tensor. It must be recalled that this criterion is only applied to the resolved scales and that the vortex shapes could be different if the whole flow field was considered. A positive value of Q highlights the regions where the rotation exceeds the strain. An example of such visualizations is depicted in figure 4 which presents an instantaneous snapshot of the flow. The high-density-gradient areas are respectively the expansion fan at the base and the recompression region. However, the recompression shock pattern appears to be much more complex than in the time-averaged point of view, denoting strong unsteady features. Numerous turbulent structures are educed thanks to the Q criterion, with the occurrence of hairpin vortices. The eddies are highly

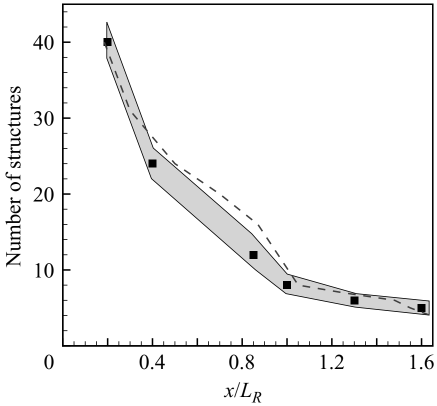

FIGURE 5. Estimation of the number of structures in the azimuthal direction (dashed line, simulation; ■, experiment; grey area, RMS experimental value).

three-dimensional and appear to grow in size farther downstream leading to a reduction of the number of vortices.

Figure 5 depicts the streamwise evolution of the number of eddies in the azimuthal direction along the shear layer and the results are compared to the experimental data of Bourdon & Dutton (2001).

Despite only one time instant being used for the present estimation, the numerical observations compare well with the experimental results and properly predict the reduction in the number of eddies as the recirculation area shrinks. This is further evidence that the simulation can be used to investigate the vortex dynamics.

Thus, the present simulation exhibits most of the features observable in the experiment and will now be used to obtain a better insight into the dynamics of the flow.

5. Mixing layer analysis for $0 < x/L_R < 0.60$

5.1. *Mean flow analysis*

The time-averaged behaviour of the free shear layer was first investigated and particular attention was paid to the mixing layer growth. Consequently, the vorticity thickness δ_ω has been used:

$$\delta_\omega(x,\theta) = \frac{\Delta U}{(\partial u(x,r,\theta)/\partial r)_{max}} \tag{5.1}$$

with $\Delta U = U_1 - U_2$.

The evolution of δ_ω behind the base is plotted in figure 6 where three distinct zones can seen. The first region just after separation extends to approximately 0.3 x/L_R and exhibits a growth rate $\mathrm{d}\delta_\omega/\mathrm{d}x$ approximately equal to 0.25. This region corresponds to the initial part of the shear layer where instabilities develop. On moving downstream, $\mathrm{d}\delta_\omega/\mathrm{d}x$ increases until reaching a value equal to 0.38. This large value departs from the classical values encountered in canonical shear layers. However, this quite high spreading rate is due to the existence of the recirculating flow which involves high turbulence levels on the low-speed side as already observed in planar incompressible separating/reattaching flows (Dandois, Garnier & Sagaut 2007) as well as in subsonic

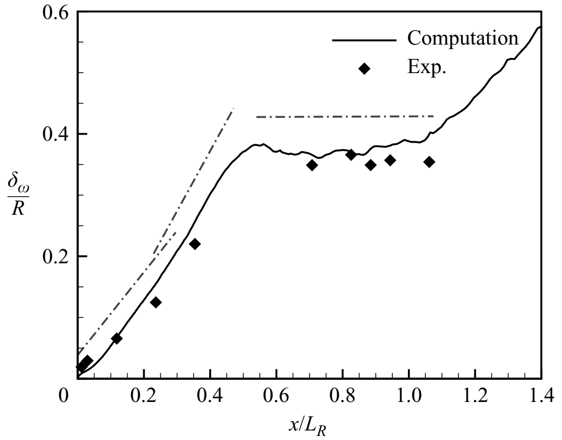

FIGURE 6. Vorticity thickness evolution along the mixing layer.

axisymmetric cases under moderate compressibility (Deck & Thorigny 2007 and Simon *et al.* 2007). For example, the latter showed that high values of the mixing layer spreading rate are also observed in massively separated base flows for projectile configurations in the subsonic and transsonic regimes. At $x/L_R \sim 0.60$, a strong change in the mixing layer evolution is observed. The vorticity thickness becomes nearly constant until the rear stagnation point at $x/L_R = 1$ is reached. This shift in the trend of the growth rate is due to the appearance of an adverse pressure gradient when the flow starts to realign with the axis as observed in figure 2. It can be noted that the numerical results agree fairly well with the experimental values extracted from the LDV data.

For canonical shear layers, the vorticiy thickness growth rate can be defined by the relation

$$\frac{\mathrm{d}\delta_w}{\mathrm{d}x} = C_\delta \frac{U_1 - U_2}{U_1 + U_2}. \tag{5.2}$$

However, due to the present configuration and the existence of recirculating flow, this formula does not strictly hold and leads to a C_δ value which is dependent upon the streamwise location (for $\mathrm{d}\delta_w/\mathrm{d}x \sim 0.38$, $C_\delta(x)$ varies from 0.14 to 0.16, the latter being the classical incompressible value for planar shear layers).

For the purpose of better understanding the turbulence field modifications, the streamwise evolution of the peak Reynolds stress magnitudes $|\overline{u_i'u_j'}|_{max}/U_\infty^2$ have been investigated. Figure 7 presents the primary shear stress and both the axial and radial components of the stress tensors.

The $-\overline{u'v'}/U_\infty^2$ component results compare fairly well with the experimental data. In accordance with the shear layer growth, the primary Reynolds shear stress magnitudes rise by a factor of 2 between $x/L_R = 0.05$ and 0.6. The onset of the recompression region appears to deeply alter the turbulence field as the primary stresses start to monotically decrease from this location. This is consistent with the observations of Herrin & Dutton (1997) and confirms that the turbulence immediately reacts to the pressure gradient which constitutes an extra strain rate, and contrasts with conclusions about subsonic flows.

The evolution of the streamwise component $\overline{u'^2}/U_\infty^2$, depicted in figure 7(*b*) can be divided into four regions. For $0.05 < x/L_R < 0.2$, it decreases by nearly 16%. Then, its magnitude remains constant until $x/L_R = 0.45$. Downstream of this point,

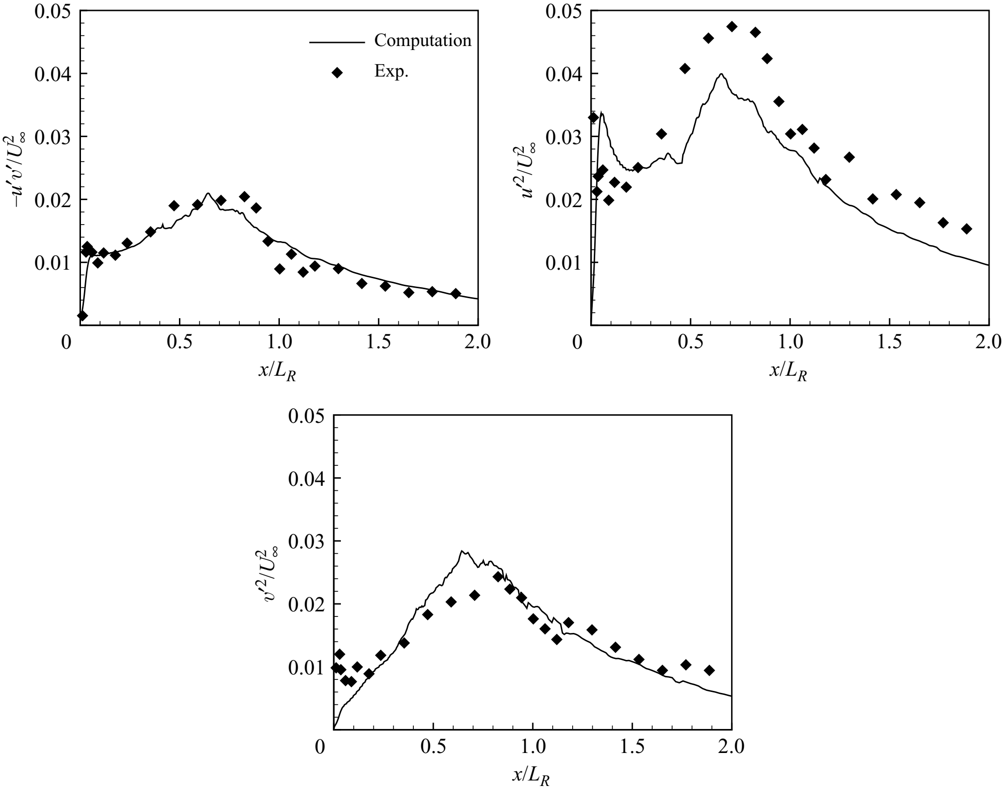

FIGURE 7. Longitudinal evolution of the peak Reynolds stresses: (*a*) $-\overline{u'v'}/U_\infty^2$, (*b*) $\overline{u'^2}/U_\infty^2$ and (*c*) $\overline{v'^2}/U_\infty^2$.

$\overline{u'^2}/U_\infty^2$ increases until the onset of recompression. Once again, the axial normal stress responds instantaneously to the adverse pressure gradient. Figure 7(*c*) presents the evolution of the radial normal stress. Its magnitude is less than that of the axial stress and corroborates the finding of the domination of streamwise velocity fluctuations in such flows (see for example Olsen & Dutton 2003; Goebel & Dutton 1990, Samimy & Elliot 1990, Urban & Mungal 2001); it exhibits a different behaviour than $\overline{u'^2}/U_\infty^2$ in the initial stage of the shear layer. The magnitude of $\overline{v'^2}/U_\infty^2$ is found to increase until the recompression point is reached. Although not shown here, both the magnitude and evolution of $\overline{w'^2}/U_\infty^2$ are similar to those of $\overline{v'^2}/U_\infty^2$.

Table 1 summarizes some interesting properties of the turbulent field encountered in classical shear flows as well as those encountered in the present simulation. It illustrates the decrease of the fluctuation magnitude with M_c in canonical shear flows while the anisotropy is found to increase.

Because of the different evolution of the peak Reynolds stresses along the mixing layer, it is interesting to investigate some particular ratios which depict the structural changes of the turbulent field due to the application of the extra strain rates. Figure 8(*a*) depicts the evolution of the Reynolds stress anisotropy through a primary-to-secondary stress ratio $(\sigma_u/\sigma_v)^2$ and a secondary-to-secondary stress ratio $(\sigma_w/\sigma_v)^2$.

These ratios, measured at the peak shear stress location, exhibit two distinct trends. The first ratio underlines the domination of the axial stress in the whole turbulent field. However, $(\sigma_u/\sigma_v)^2$ is nearly equal to 3 downstream of separation and quickly decays to

	Topology	EXP	SIM	M_c	$u_{rms}/\Delta u$	$v_{rms}/\Delta u$	$\sqrt{\overline{u'v'}}/\Delta u$	v_{rms}/u_{rms}	$\sqrt{\overline{u'v'}}/u_{rms}$
Friedrich & Arnal(1990)	BFS		x	–	0.224	0.141	0.126	0.629	0.562
Bell & Mehta (1990)	PML	x		∼0.00	0.18	0.14	0.10	0.777	0.555
Jovic (1996)	BFS	x		∼0.02	0.2	0.148	0.122	0.74	0.61
Olsen & Dutton (2003)	PML	x		0.02	0.18	0.16	0.10	0.888	0.555
Chandsruda & Bradshaw (1981)	BFS	x		∼0.04	0.173	0.118	0.105	0.682	0.607
Goebel & Dutton (1990)	PML	x		0.20	0.22	0.15	0.13	0.682	0.593
Freund, Lele & Moin (2000)	AML		x	0.20	0.195	0.138	0.105	0.708	0.538
Urban & Mungal (2001)	PML	x		0.25	0.17	0.13	0.109	0.765	0.644
Pantano & Sarkar (2002)	PML		x	0.3	0.17	0.134	0.103	0.788	0.606
Olsen & Dutton (2003)	PML	x		0.38	0.19	0.13	0.10	0.684	0.526
Goebel & Dutton (1990)	PML	x		0.46	0.17	0.17	0.10	0.588	0.588
Samimy & Elliot (1990)	PML	x		0.51	0.16	0.11	0.089	0.687	0.556
Urban & Mungal (2001)	PML	x		0.63	0.16	0.09	0.089	0.562	0.556
Samimy & Elliot (1990)	PML	x		0.64	0.15	0.10	0.088	0.666	0.586
Goebel & Dutton (1990)	PML	x		0.69	0.18	0.078	0.083	0.429	0.461
Pantano & Sarkar (2002)	PML		x	0.70	0.153	0.103	0.087	0.673	0.568
Urban & Mungal (2001)	PML	x		0.76	0.151	0.082	0.088	0.543	0.583
Goebel & Dutton (1990)	PML	x		0.86	0.18	0.065	0.081	0.365	0.45
Freund, Lele & Moin (2000)	AML		x	0.99	0.190	0.088	0.086	0.463	0.453
Goebel & Dutton (1990)	PML	x		0.99	0.18	0.053	0.076	0.283	0.422
Pantano & Sarkar (2002)	PML		x	1.10	0.141	0.095	0.083	0.674	0.588
Freund, Lele & Moin(2000)	AML		x	1.80	0.205	0.055	0.063	0.268	0.307
Present simulation			x		0.140	0.117	0.106	0.836	0.714

TABLE 1. Comparison of peak Reynolds stresses in classical shear flows: PML denotes planar shear layer, AML axisymmetric mixing layer, and BFS backward-facing step

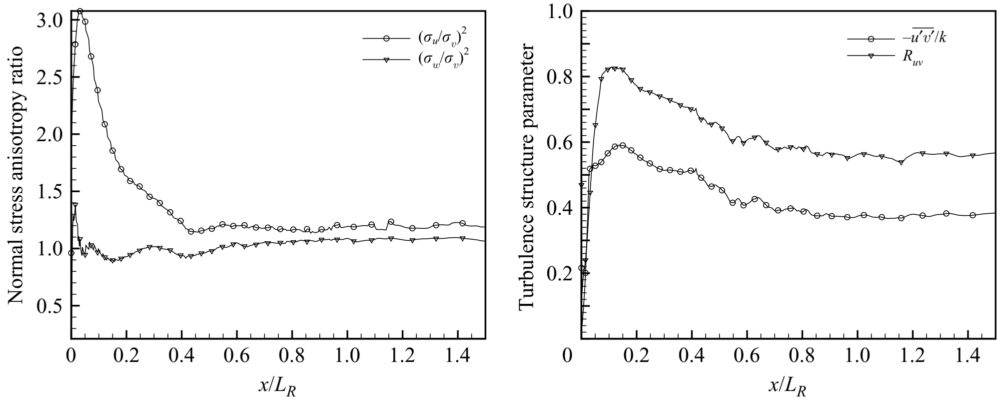

FIGURE 8. Longitudinal evolution of the normal shear stress anisotropy (*a*) and of the turbulence structure parameter (*b*) along the mixing layer.

approximately 1.2 at $x/L_R = 0.5$, denoting a larger growth of the radial fluctuations compared to the longitudinal ones. Farther downstream, this value remains constant through the recompression process and the developing wake, assuming that some equilibrium state has been reached. The 1.2 value is significantly lower than in planar shear layers mentioned in table 1. However, in the present case, both high- and low-speed stream characteristics evolve in the streamwise direction due to the existence of the recirculating flow. Such spatial evolution greatly differs from canonical mixing layers. In addition, the low-speed side is altered by the existence of the recirculation

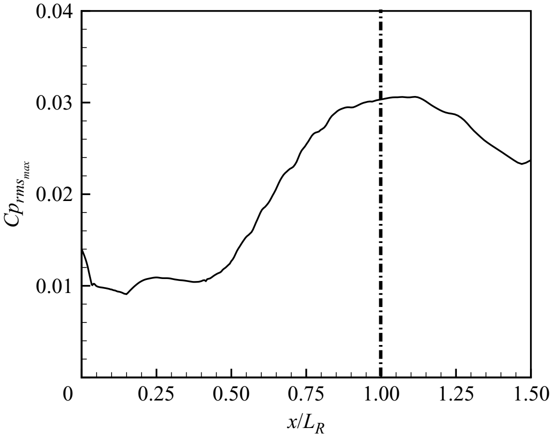

FIGURE 9. Streamwise evolution of the maximum pressure fluctuations coefficient $Cp_{rms_{max}}$ in the mixing layer.

area which enhances its turbulence level. Owing to these considerations, a strict comparison between the axisymmetric and the planar cases is quite difficult. The second ratio, $(\sigma_w/\sigma_v)^2$, remains nearly constant along the mixing layer independently of the additional strain rates. Its value is slightly larger than 1 in accordance with the results of Herrin & Dutton (1997) in the case of an axisymmetric, boat-tailed trailing edge.

In addition to the normal shear stress distribution, some others relevant ratios can be studied. As stated by Herrin & Dutton (1997), shear-stress-to-normal stress ratio may be used for Reynolds stress closure. Two turbulence structure parameters are plotted in figure 8(*b*). The first ratio is $-\overline{u'v'}/k$ where k is the turbulent kinetic energy defined as $k = (\sigma_u^2 + \sigma_v^2 + \sigma_w^2)/2$. The second one, commonly called the shear stress correlation coefficient, is $R_{uv} = (-\overline{u'v'})/(\sigma_u \sigma_v)$. Both ratios exhibit the same evolution despite different magnitudes. A strong decay is observed until $x/L_R = 1$ and an asymptotic level is then reached. This contrasts with the experimental observation of Herrin & Dutton (1997) where no equilibrium state is reached at least until $x/L_R = 1.5$ when a boat-tailed trailing edge is used to generate the annular mixing layer. The $-\overline{u'v'}/k$ ratio has a constant value of 0.4 which is slightly higher than the value of 0.3 recommended by Harsha & Lee (1970) for turbulent flow calculations. The R_{uv} ratio magnitude of approximately 0.6 agrees well with the results of Urban & Mungal (2001) for $M_c = 0.63$.

To conclude the study of the mean properties of the shear layer before entering the recompression region, the maximum of the pressure fluctuations have been investigated and plotted in figure 9. It can be seen that pressure fluctuation maxima are nearly constant for $0 < x/X_R < 0.5$ with $Cp_{rms_{max}} \sim 0.01$. This behaviour differs from those observed in subsonic compressible base flows such as in Deck, Garnier & Guillen (2002), where the pressure maxima quickly increase during the early stages of development of the shear layer and reach a value of approximatly 0.07 (for $M_\infty = 0.7$), which is much higher than the constant value observed in the present case.

5.2. *Coherent structure dynamics*

In the previous section, the turbulence field has been investigated by means of the time-averaged data and its behaviour has been highlighted. Instantaneous data

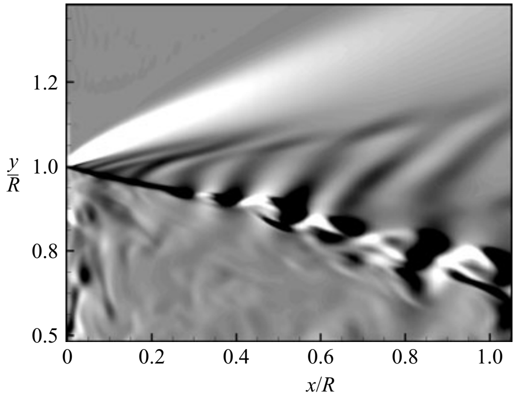

FIGURE 10. Visualization of radiating pressure waves on the upper side of the vortices educed using $\partial\rho/\partial x$.

will now be used to investigate the turbulence properties through the existence and evolution of coherent vortices along the mixing layer.

The initial stage of the shear layer is first investigated. Figure 4 depicts the iso-surface of the Q criterion. The present case differs from the incompressible shear layer cases where large spanwise rollers are observed due to the domination of the classical KH instability. The small scales appear to be highly three-dimensional. Indeed, after separation, the compressibility effects are strong and the local convective Mach number is greater than 1. It has been demonstrated (see for example Sandham & Reynolds 1991) that the shear layer is no longer dominated by the Kelvin–Helmholtz instability. When $M_c > 1$, oblique modes dominate the instability process, leading to small-scale three-dimensional structures. The angle of the structure with the axis of the mean flow is dependent on the M_c value. Sandham & Reynolds (1991) have used the linear stability theory to educe a relation between M_c and the preferred mode for planar shear layers:

$$M_c \cos(\theta) \sim 0.6. \tag{5.3}$$

Even though an averaged structure angle has not been clearly found in the simulation, the visualization of figure 4 clearly shows highly three-dimensional vortices, inclined toward the axis and with a weak azimuthal coherency.

The streamwise derivative of the density is used to show the vicinity of the separation process in figure 10. The white area depicts the expansion fan centred at the base which deflects the separating boundary layer. It is obvious that coherent vortices exist in the shear layer just downstream of the base. Further evidence of their existence is found in the pressure waves emanating from their upper side. Some eddies are seen along the trailing edge and a small recirculation area is educed in the outer part of the base. These observations are consistent with the strong growth rate of the mixing layer which can be forced by the impact of vortices coming from the recirculation bubble.

As the existence of coherent vortices has been demonstrated in the developing shear layer, it is of primary interest to investigate their convective velocity U_c in order to estimate the relevance of the isentropic model of U_c. An estimation of the isentropic convective Mach number M_c has been plotted in figure 11 and compared to the experimental values. The convective velocity has also been estimated with the use of

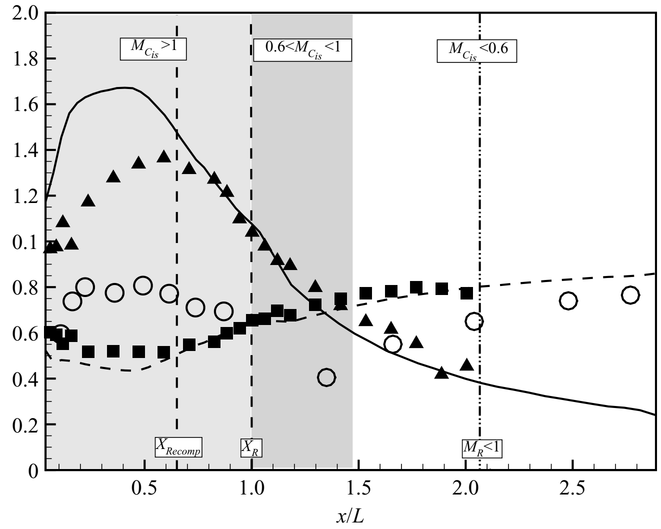

FIGURE 11. Streamwise evolution of the coherent structures dynamics (solid line, $M_{c_{is}}$ from computation; ▲, $M_{c_{is}}$ from the experiment; dashed line, $U_{c_{is}}$ from the computation; ■, $U_{c_{is}}$ from the experiment; ○, U_c computed from two-point–two-time correlations).

the isentropic model:

$$U_c = \frac{a_2 U_1 + a_1 U_2}{a_1 + a_2}. \tag{5.4}$$

Lastly, the calculated convective velocities (using two-point–two-time correlations) have been added. In the present section, the analysis will only focus on the mixing layer behaviour for locations $0 < x/L < 0.60$ and the other parts of the flow will be discussed in subsequent sections. The convective Mach number exhibits an identical trend for simulation and experiment despite a higher value in the initial stage of the mixing layer. In both cases, M_c is greater than 1 until $x/L = 0.60$ is reached, which denotes a high compressibility level in the shear layer. The isentropic model leads to convective velocity $U_{c_{is}}$ values of nearly $0.5U_\infty$ which is equal to those encountered in flows with $M_c < 1$ such as cavity or backward-facing step configurations. Two-point–two-time correlations are used to measure the real convective velocities. The structures are found to quickly accelerate over a short length to reach a constant value nearly equal to $0.8U_\infty$ for $0.2 < x/L < 0.60$. This value is greatly higher than the predictions given by the isentropic model and is in accordance with fundamental work on supersonic planar shear layers. As the upper side of the shear layer is supersonic, in contrast to the subsonic lower side, the mixing layer is convectively unstable toward the fast mode (also called the supersonic mode). The behaviour of the present axisymmetric mixing layer is thus close to that of two-stream supersonic–subsonic shear layers at identical M_c. However, the present result contrasts with the experimental measurements of Thurow *et al.* (2003) who observed both slow and fast modes in a round jet at high M_c.

According to the previous results, the isentropic model fails to predict the convective velocity in the present case. Figure 12 displays M_{c_2} values versus M_{c_1} along the mixing layer in order to show the departure of the flow from the isentropic assumptions which lead to $M_{c_1} = M_{c_2}$. It is obvious that the present physics greatly differs from the

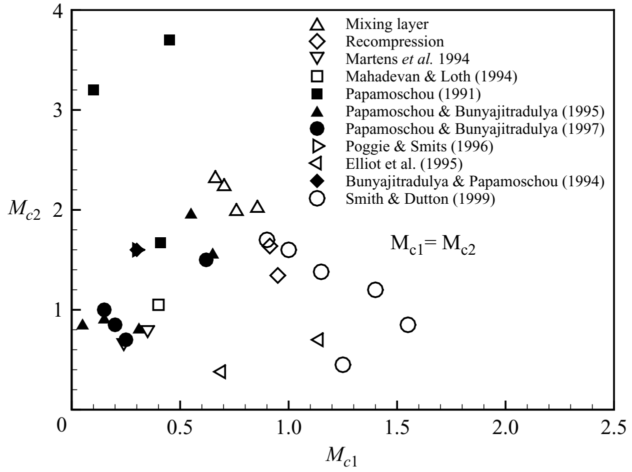

FIGURE 12. Departure from the isentropic convective Mach number theory: results of previous work on supersonic/subsonic shear layers have been included.

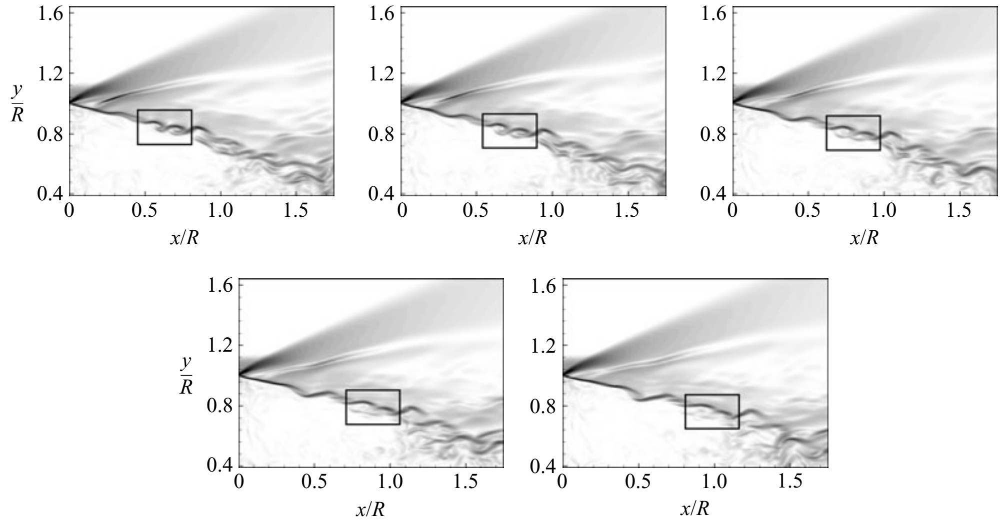

FIGURE 13. Convection and merging of coherent structures in the free shear layer $(0 < x/L_R < 0.65)$ educed using iso-contours of $||\mathrm{grad}(\rho)||$: instantaneous snapshots $\Delta t = 3.3 \times 10^{-6}$ s apart from top left to bottom right.

isentropic model in conjunction with the high values of M_c and agree well with the results of previous studies on supersonic–subsonic shear layers.

Visualizations of the educed vortices convected at supersonic speeds are given in figure 13 by iso-contours of $\|\mathrm{grad}(\rho)\|$. In these side views, the eddies appear to have an elliptical shape with their major axis inclined toward the mixing layer axis. These structures are convected without strong structural changes as their exis tence is obvious in the first three successive instantaneous snapshots, in accordance with the experimental results reported by Bourdon & Dutton (1999). Farther downstream, the vortices exhibit some merging which differs from the classical rotational pairing responsible for the subsonic mixing layer growth. In fact, three-dimensional

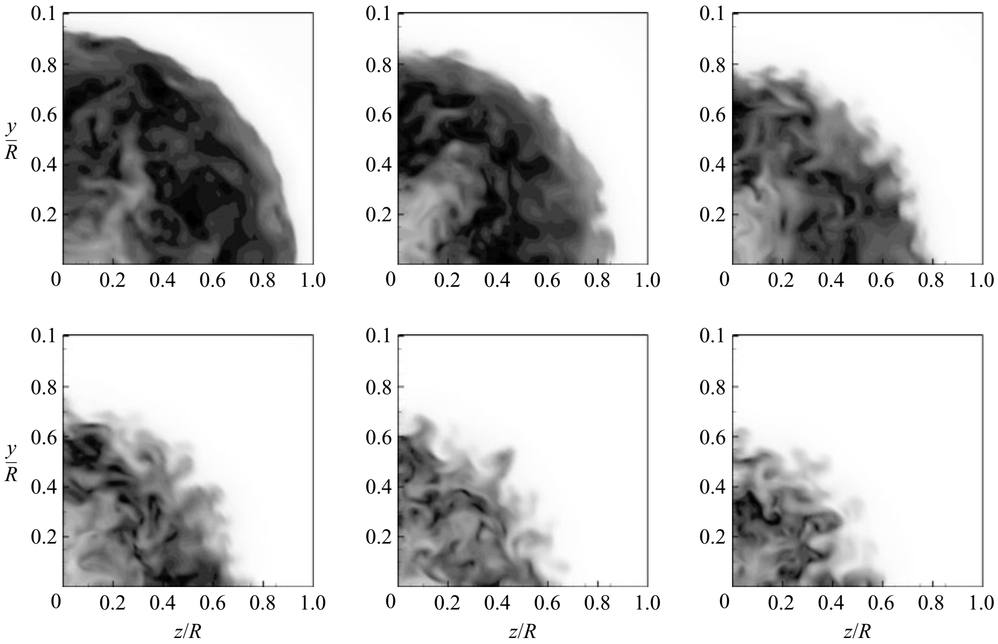

FIGURE 14. Instantaneous end views of iso-contours of the Mach number in the near wake ($0 < x/L_R < 0.60$). From top left to bottom right, each picture is translated by $0.1 \times x/L_R$.

animations of the Q criterion reveal that the primary oblique vortices realign with the longitudinal axis on being convected downstream and then merge in a complex process as depicted in figure 13. This coalescence phenomenon occurs upstream of the recompression region where the peak magnitude of $-\overline{u'v'}/U_\infty$ increases (see figure 7). The realignment of the oblique eddies in the streamwise direction while they are convected is consistent with the increase in their major axis observed by Bourdon & Dutton (1999) when looking at the vortices in a planar view.

In addition to the previous side-views, end-views are used to investigate the occurrence of coherent vortices in the azimuthal direction. Such visualizations are depicted in figure 14 where each picture is offset by $0.1 \times x/L_R$. Only one-quarter of the recirculating area is plotted to better show the azimuthal distribution of the eddies. In the first two pictures, no longitudinal vortices can be seen in accordance with figure 4 as this area is dominated by oblique modes. On moving farther downstream, mushroom-shape structures arise which corroborates the planar visualizations of Bourdon & Dutton (1999) and give further evidence of the existence of streamwise vortices. Their number is found to decrease as the recirculation area shrinks due to the initial deflection of the shear layer during the separation process.

Herrin & Dutton (1995) have performed an analysis of the instantaneous shear stress angle Ψ, where $\Psi = \arctan(v'/u')$ in order to show the evolution of the Reynolds stress distribution in the light of the previous visualizations. This investigation has been performed for two different streamwise stations corresponding respectively to the appearance of streamwise vortices and to a location just ahead of the onset of recompression.

Figure 15 depicts the probability density function (PDF) of Ψ for the two streamwise stations (N/N_T represents the normalized number of samples). In figure 15(a), preferentially negative Ψ values, corresponding to Q2 and Q4 events in a quadrant

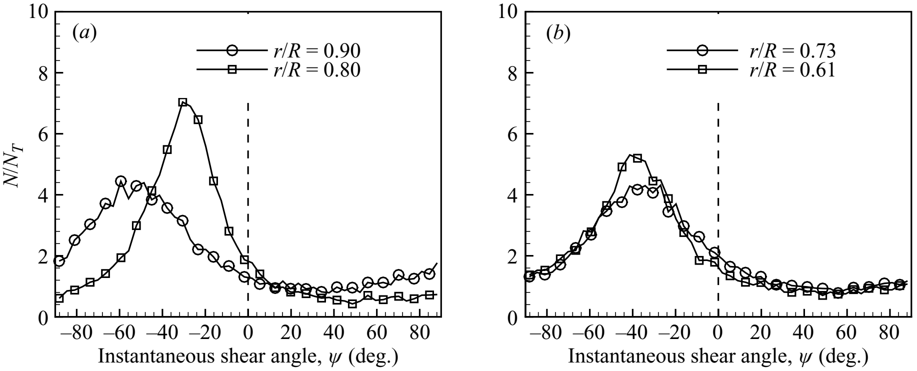

FIGURE 15. PDF of the instantaneous shear angle Ψ past separation ($x/R = 0.79$) (a) and just ahead of recompression ($x/R = 1.28$) (b) in the mixing layer.

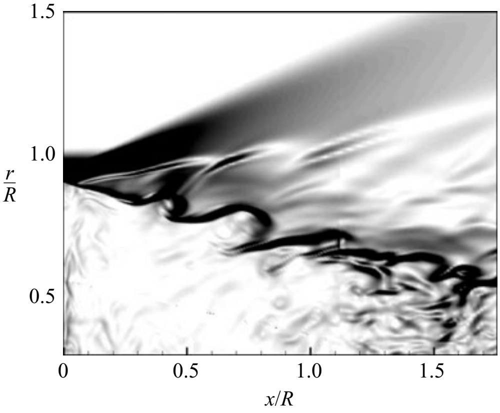

FIGURE 16. Visualization of a large-scale coherent structure originating from the first stage of the mixing layer shown with iso-contours of $||\mathrm{grad}(\rho)||$.

decomposition, are observed. However, the Ψ distribution appears to be highly sensitive to the radial location of measurement. A strong orientation of the shear stress of around 30° is observed in the inner part of the mixing layer whereas a more broadband distribution centred around nearly 55° is encountered on approaching the high-speed side (a strong dependence upon the radial location has also been observed by Clemens, Petullo & Dolling (1996) for a confined supersonic shear layer at low M_c). Further downstream, the difference between the lower and upper sides of the free shear layer is reduced. This is consistent with the growth of the vortices on convection downstream and with the amalgamation of the structures previously highlighted. These results are consistent with those of Herrin & Dutton (1997) achieved in the case of a boat-tailed afterbody.

To conclude the investigation of the dynamics of the vortices in the initial part of the mixing layer, planar and full three-dimensional animations have been used to educe the existence of large-scale structures. According to Bourdon & Dutton (2000), an apparent flapping motion of the shear layer is caused by the convection of very large-scale vortices along the mixing layer, leading to an asymmetry in the instantaneous pressure distribution in the azimuthal direction. Such eddies have also been found among all the instantaneous data as it can be seen in figure 16 (the scale is identical to that used in figure 13 to allow comparison of the structure size).

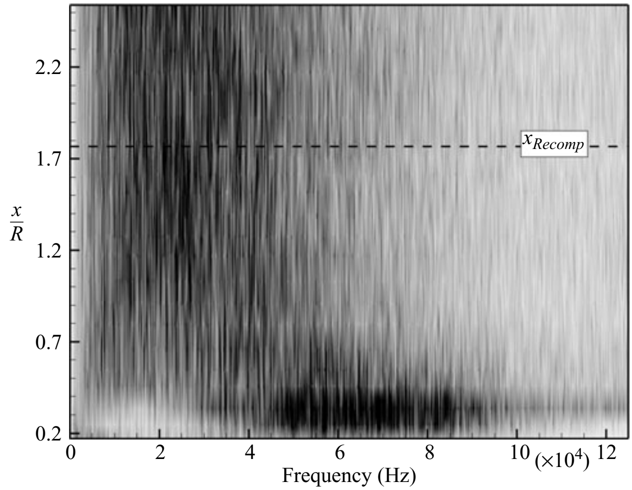

FIGURE 17. Spectral surface of longitudinal velocity fluctuations $(G_u(f) * f/\sigma_u^2)$ along the mixing layer.

Such an eddy is significantly larger than the vortices educed in figure 13 and corroborates the experimental findings. However, no clear periodic nature in their occurrence has been found and a spectral analysis is required in order to show possible periodic motions in the mixing layer.

5.3. *Spectral analysis*

Some additional knowledge can be obtained by performing a spectral analysis of the mixing layer. Such an investigation has been performed by plotting the spectral surface of the longitudinal velocity fluctuations along the mixing layer using 23 sensors in figure 17.

The present analysis focuses on the mixing layer behaviour ahead of the recompression. Two distinct areas can be seen: downstream of separation, the initial stage of the shear layer displays a high-frequency content corresponding to the primary instability of the mixing layer unlike downstream locations where the spectral content is pushed toward lower frequencies in accordance with the growth and amalgation of the convected vortices along the shear layer.

Two characteristic spectra coming from the previous spectral surface can be seen in figure 18. Figure 18(*a*) depicts a spectrum of velocity fluctuations downstream of separation. As mentioned earlier, the high-frequency content, centred around approximately 60 kHz, is the signature of the instability process of the shear layer. This frequency is also encountered in the radial velocity fluctuation spectra and in the temporal autocorrelation coefficients. However, it is obvious that, at this location, the shear layer has a low-frequency component. A peak is observed at 1350 Hz ($St_D \sim 0.144$) but energy is relatively constant until 700 Hz. A similar frequency is observed in radial and tangential velocity spectra despite the lower value of 900 Hz ($St_D \sim 0.096$). This quite low frequency does not scale with the mixing layer properties and may be characteristic of a global behaviour of the whole flow just downstream of separation. As previously discussed, a flapping motion of the shear layer is a good candidate for this frequency.

Figure 18(*b*) exhibits the longitudinal velocity spectrum just ahead of recompression in the mixing layer. It is observed that the high-frequency component has spread to

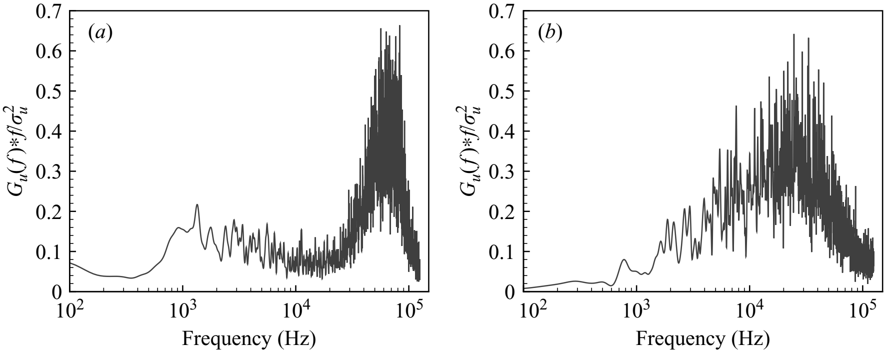

FIGURE 18. Longitudinal velocity spectra (*a*) in the initial part of the mixing layer for $x/R = 0.25$ and $y/R = 0.97$ and (*b*) ahead of the recompression region for $x/R = 1.52$ and $y/R = 0.61$.

lower frequencies corresponding to the growth of the vortices as they are convected. The spectrum exhibits a broadband shape with maximum fluctuations around 25 kHz (this value is a little higher for the radial and tangential velocity fluctuations). In addition, a small peak is observed at a frequency corresponding to 800 Hz ($St_D \sim 0.085$). Movements of the whole separated flow enclosed in the annular shear layer have been experimentally observed for frequencies below 1 kHz (Cannon *et al.* 2005). The present work gives further evidence of the existence of such large-scale behaviour.

To summarize, the present section is devoted to the mixing layer properties ahead of the recompression. An investigation of the time-averaged flow field has highlighted the strong growth rate of the shear layer coupled with a domination of the streamwise velocity fluctuations. Instantaneous samples have demonstrated the existence of numerous turbulent scales. As a result of the compressibility of the flow, the isentropic model of the convective Mach number fails to predict the vortex dynamics which appear to be linked to the supersonic mode. A spectral analysis gives the frequency of the shear layer instability as well as a low-frequency phenomenon which appears to be related to a flapping motion of the mixing layer. The next section will assess the shear layer properties during the recompression process as well as the dynamics of the complex shock pattern educed in figure 4.

6. Turbulence structure in the recompression and in the rear stagnation region ($0.6 < x/L_R < 1$)

6.1. *Mean flow analysis*

On moving downstream, the free shear layer develops closer to the axis and the axisymmetrical constraints increase. For $x/L_R > 0.65$, the lateral streamline convergence leads to recompression and to the formation of a compression shock from a time-averaged point of view as depicted in figure 2. The incoming fluid particles having enough momentum pass through the recompression and then are convected downstream into the developing wake. Those with less energy are pushed upstream into a backflow area which will be discussed in the last section.

The recompression process has a direct effect on the shear layer behaviour as highlighted by the evolution of δ_ω (see figure 6). A constant value of δ_ω is observed until the rear stagnation point is reached, providing some evidence of the turbulence

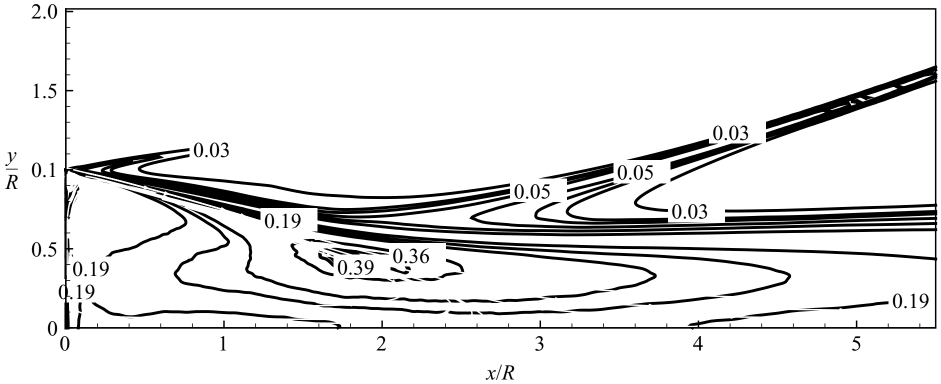

FIGURE 19. Turbulent Mach number field based on the resolved turbulent kinetic energy.

field alteration. As observed in figure 7, the recompression region represents the onset of the velocity fluctuation decrease. The parameter quantifying the compressibility influence on the turbulent fluctuations is the turbulent Mach number M_t which can either be defined with a root-mean-square (RMS) value of the longitudinal velocity fluctuation $(u'^2)^{1/2}/a$ or with the resolved turbulent kinetic energy $(\tilde{k})^{1/2}/a$. Figure 19 displays the M_t distribution and in particular non-negligable values in the recirculating area since M_t can reach values as high as 0.20. Moreover, its highest values are found in the recompression region where M_t has values up to 0.36 or 0.40 depending on the scaling. At the present M_t levels ($M_t < 0.6$) and according to Erlebacher *et al.* (1992), the subgrid kinetic energy can be lumped with the pressure term as mentioned in § 3.2.

The longitudinal and radial fluctuation components exhibit the same behaviour when passing through the recompression, allowing a constant value of the anisotropy parameter $(\sigma_u/\sigma_v)^2$ approximately equal to 1.25 due to the domination of the streamwise fluctuations (see figure 7 and figure 8). Thus, the turbulence field intensity decreases while the anisotropy of the flow remains constant. This is a quite different behaviour from that encountered in compressible turbulent reattaching free shear layers such as in compression ramp configurations. On approaching the ramp, the free mixing layer enters a compression region leading to a modification of the turbulence field. The velocity fluctuations are immediately enhanced and maximum fluctuations levels are reached just downstream of the mean reattachment point (Samimy, Petrie & Addy 1986).

Finally, the pressure gradient resulting from the streamline curvature coupled with density variations is responsible for another particular property of the present configuration. One characteristic feature of compressible flows is the vorticity generation due to the baroclinic term in the vorticity transport equation. In the present case, the adverse pressure gradient is not aligned with the density variations across the shear layer, which only appear in the radial direction. Thus, this area appears as a source of vorticity through the compressible term of the equation. Iso-contours of the baroclinic torque magnitude are compared to the vortex stretching/tilting term in an instantaneous snapshot (figure 20). It is obvious that the compressibility acts not only in the recompression region but also during the whole mixing layer development and its effect on the vorticity generation is of the same order as the incompressible source term, at least in the shear layer.

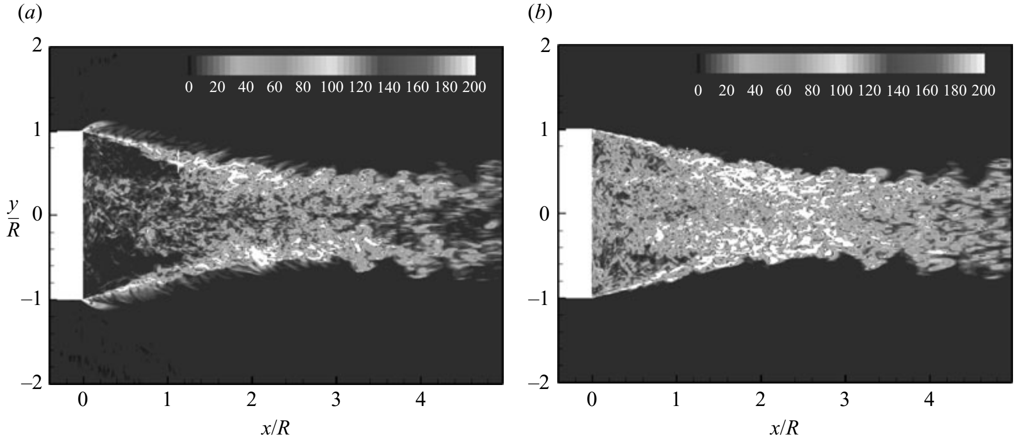

FIGURE 20. Iso-contours of source term magnitude in the vorticity transport equation. (a) Baroclinic torque: $\rho^{-2}\|\mathrm{grad}(\rho)\wedge\mathrm{grad}(p)\|$, (b) vortex stretching/tilting $\|\boldsymbol{\Omega}_j\partial u_i/\partial x_j\|$.

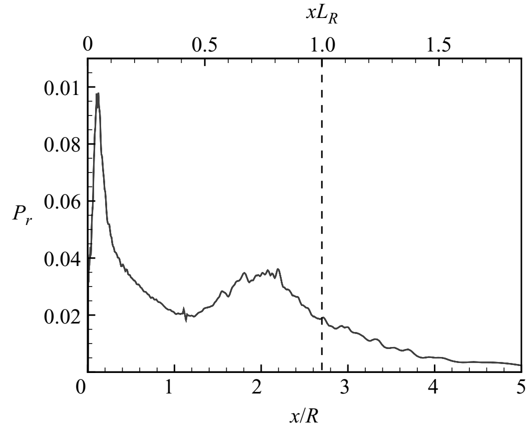

FIGURE 21. Maximum of turbulent kinetic energy production extracted from the mean flow - $P_r = -\widetilde{\rho u'_i u'_j}\frac{\partial \widetilde{u'_i}}{\partial x_j}$.

The influence of the adverse pressure gradient and streamline curvature can also be observed by scutinizing the production of the turbulent kinetic energy. The evolution of its maximum has been tracked and is plotted in figure 21. A narrow peak can be observed in the initial stage of the shear layer in accordance with the occurrence of the instability process. As the mixing layer develops, the production magnitude decreases. However, on entering the recompression region, a second and wider peak can be seen, demonstrating the influence of the extra strain rates on the turbulent production whereas the reattachement process and the wake involve a decrease of the production term.

6.2. *Coherent structures dynamics*

The complexity of the recompression shock pattern has been highlighted in figure 4, and so the unsteady properties of the foot shock have been assessed from an animated movie. Five successive snapshots of the flow are displayed in figure 22,

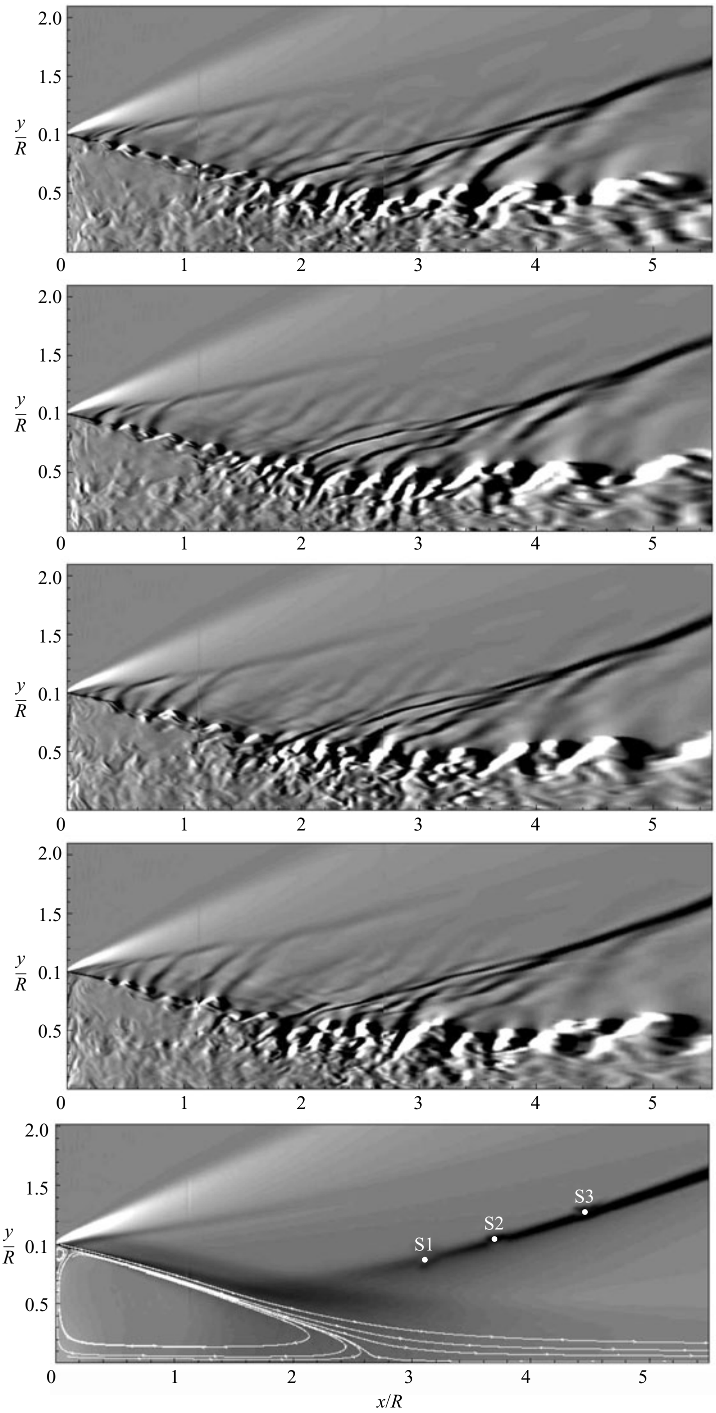

FIGURE 22. Visualizations of the foot shock unsteadiness educed by iso-contours of $\partial\rho/\partial x$. Each picture is $\Delta t = 2.64 \times 10^{-5}$ s apart from top left to bottom right. The last picture represents the time-averaged flow field, the computed streamlines and the sensor locations across the shock.

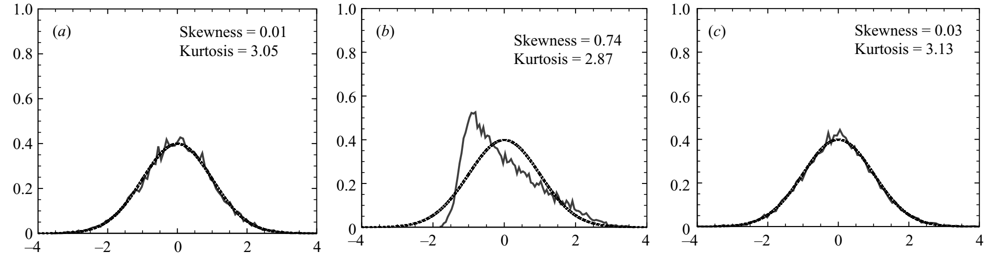

FIGURE 23. PDF of pressure signals for the three sensors: (*a*) S1, (*b*) S2, (*c*) S3 (solid line) the Gaussian distributions (dotted line) have been added for reference.

$\Delta t = 2.64 \times 10^{-5}$ s apart. These pictures present the longitudinal derivative of the density, highlighting the high density gradient regions.

The last image, depicting the mean flow field, has been added to the compare two points of view and show the shortcomings of the time-averaged one. On the instantaneous pictures, two distinct zones can be highlighted: the shock foot which is formed by several Mach waves and the recompression shock in the free stream. As already observed for the Mach waves in figure 10, shocks emanate from the upper side of the vortices and are convected at the same velocity through the recompression. This is evidence of the supersonic speed of the eddies compared to the local speed of sound a. On penetrating the free stream, they coalesce into an oblique shock which appears quite steady.

Such observations have also been made in shock/boundary layer interaction (SBLI) studies (see the review by Dolling 2001). The shock foot has been found to oscillate due to shocks linked to the coherent structures of the incoming turbulent boundary layer (Poggie & Smits 2001; Wu & Miles 2001). This particular behaviour involves a high sensitivity of the foot region to the incoming flow disturbances.

To further investigate the behaviour of the shock pattern, the PDF of the pressure has been assessed for several sensors located across the recompression shock (see figure 22).

Figure 23 depicts the PDF of the pressure signals for the S1, S2 and S3 sensors and the third- and fourth-order moments values have been added. S1 and S3 exhibit the same behaviour with a quasi-perfect Gaussian shape. However, the S2 sensor displays a quite different behaviour with a strong departure from the Gaussian reference. The PDF is no longer symmetric, with a skewness coefficient equal to 0.74 (compared to the 0 value of the classical Gaussian shape) while the kurtosis coefficient is slightly less than 3. This finding may be evidence of a global motion of the shock and will be further assessed with the use of a spectral analysis in the next section.

Both isentropic assumptions and two-point–two-time correlations have been used to estimate the convection velocity of the structures on passing through the recompression. The results have been plotted in figure 11. Both experimental and numerical isentropic predictions agree extremely well. $M_{c_{is}}$ decreases from 1.4 to nearly 1 at location $x/L_R = 1$. The estimated $U_{c_{is}}$ is found to only increase by nearly 30%. The use of the correlation coefficients reveals a completely different trend. As the fast mode dominates the instability process, the convective velocity of the incoming vortices is higher than the isentropic value on entering the recompression but is found to slightly decrease when passing through the recompression. Consequently for the time-averaged investigation, magnitude of $\overline{u'^2}$ drops, leading to a decrease of k and

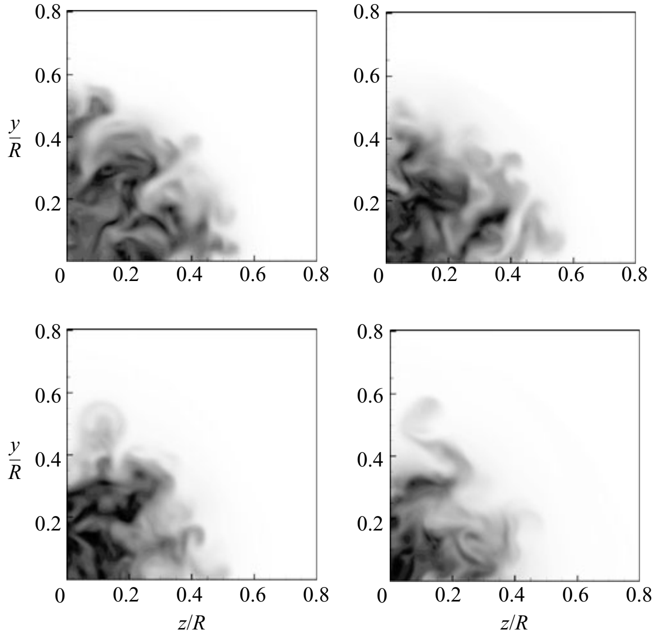

FIGURE 24. Instantaneous end views of iso-contours of Mach number in the recompression region ($0.70 < x/L_R < 1$). Each picture is offset by $0.1 \times/L_R$ from top left to bottom right.

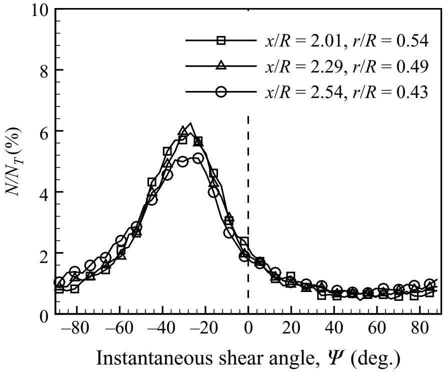

FIGURE 25. PDF of the instantaneous shear stress angle Ψ along the mixing layer in the recompression region.

thus to a deceleration of the eddies. This result underlines the shortcomings of the isentropic model when a pressure gradient occurs in the flow field.

In addition to the side views previously described in figure 22, end views of iso-Mach numbers are also presented in figure 24. As the enclosed area shrinks, the number of mushroom-shape structures decreases as demonstrated in an experiment (Bourdon & Dutton 1999) and in accordance with the observations during the mixing layer analysis. The large-scale structures have a distorted shape allowing a great amount of external fluid to be engulfed into the shear layer and the mixing process is then enhanced due to the three-dimensionality of the fluctuations.

Additional knowledge of the turbulence structure can be obtained by plotting the PDF of the instantaneous shear angle Ψ. Figure 25 presents the results for the

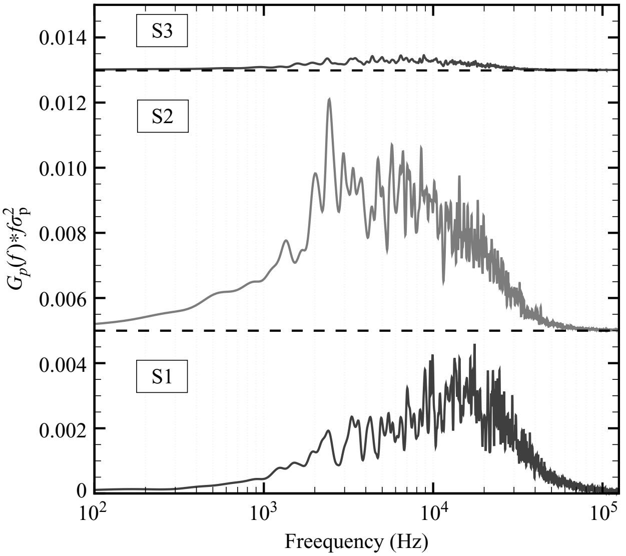

FIGURE 26. Pressure spectra $G_p(f) * f/\sigma_p^2$ for the recompression shock pattern.

recompression area. An identical shape is observed for three different points in the recompression region. The PDFs exhibit a preferential Ψ angle of nearly 28°. However, the PDFs appear to be more broadband than those upstream of the pressure gradient (see figure 15*a*). This is consistent with a loss of coherence when passing through the recompression region.

6.3. *Spectral analysis*

The dynamics of the recompression shock pattern has been investigated with pressure time series for several locations.

Figure 26 presents the pressure spectra for the three sensors S1, S2 and S3, already used for the PDFs. The S1 spectrum exhibits a broadband high-frequency content. At this location, the flow is dominated by the Mach waves emanating from the convected large-scale structures of the shear layer as observed in figure 22. The S2 sensor is located above the shock foot region where all the pressure waves coalesce to form an oblique shock. The low- and (mainly) mid-range frequency content increases. However, a distinct peak is observed for a frequency, denoted f_{SH}, equal to 2440 Hz. This quite low frequency, compared to the turbulent scales of the mixing layer, defines a large-scale shock motion. A rough estimate of the incoming shear flow frequency can be made with the use of characteristic velocity and spatial scales. Thus, the expression $f_{ML} = U_c/\delta_\omega$ leads to a frequency of nearly 34 kHz. The ratio f_{SH}/f_{ML} is found to be on the order of 0.07. It can be Note that large-scale shock motions around this typical reduced frequency has also been reported by Dolling & Murphy (1983) on a turbulent compression ramp flow.

To conclude the study of the recompression process, a spectral analysis along the mixing layer has been performed. Figure 27 presents a characteristic longitudinal velocity spectrum in the mixing layer under the constraint of an adverse pressure gradient. A large high-frequency content, centred around 30–40 kHz, is observed. However, although not shown here, the power spectral densities (PSD)s of sensors in the recompression region all exhibit a peak at approximately 800 Hz in accordance with the previous discussion dealing with the flapping motion.

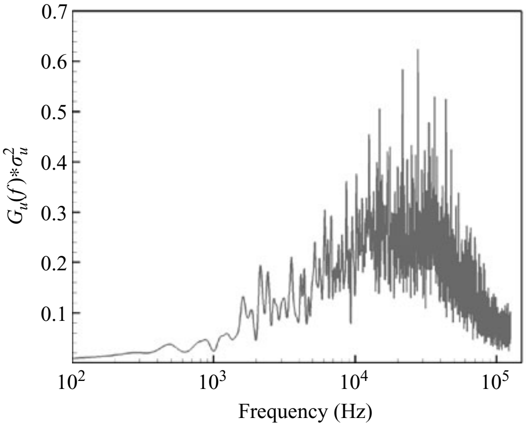

FIGURE 27. Longitudinal velocity spectra in the recompression region of the mixing layer at $x/R = 2.17$ and $r/R = 0.52$.

In summary, an investigation of the recompression process has shown that the additional strain rate resulting from the lateral streamline convergence deeply alters the turbulent field. The primary shear stress magnitude drops, as well as both the axial and radial velocity fluctuations, whereas the $(\sigma_u/\sigma_v)^2$ ratio remains constant. From an instantaneous point of view, the shock pattern is revealed to be complex, with the shock foot formed by convected shocks emanating from the eddies contained in the shear layer. The vortex velocity is found to be reduced through the recompression in contradiction with the prediction of the isentropic model. Finally, evidence of the existence of a large-scale motion of the shock has been presented. Attention will now turn to the investigation of the developing wake.

7. Wake region

7.1. *Mean flow analysis*

The present section is focused on the transition region between the mixing layer and the fully developed turbulent wake as far-field supersonic wakes are already known to behave in a self-similar manner. As depicted in figure 7, velocity fluctuations continue to decay in the near wake while the anisotropy ratio remains constant (figure 8). Thus, the turbulent field seems to slowly evolve to an asympotic state corresponding to a fully developed supersonic wake. This transition is accompanied by a reduction of the compressibility level which can be shown with the relative Mach number M_r parameter. M_r represents an estimation of the compressibility constraints of wakes (similarly to M_c for shear layers) and is given by

$$M_r = \frac{U_\infty - U_{axis}}{a_\infty}. \tag{7.1}$$

Figure 28 depicts the streamwise evolution of M_r in the developing wake after the rear stagnation point. The M_r value quickly drops meaning that the centreline velocity significantly accelerates over a short distance. Beyond $x/R \sim 5.5$, M_r is less than 1 and keeps decreasing. As M_r drops, the compressibility level decreases so that the wake properties should rapidly tend to those of its incompressible counterpart and reach a self-similar state.

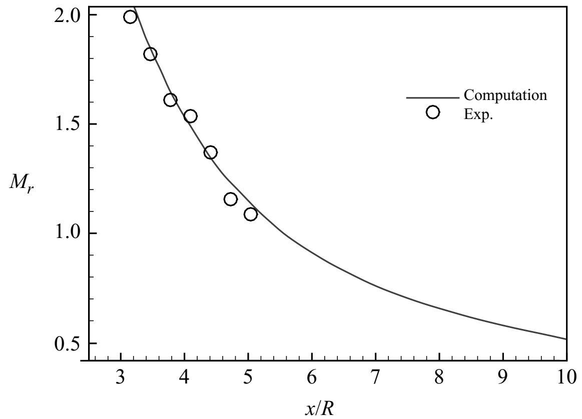

FIGURE 28. Evolution of the relative Mach number M_r in the developing turbulent wake.

7.2. *Coherent structures dynamics*

The decrease of the compressibility during the transition stage also appears in the evolution of $M_{c_{is}}$ (see figure 11). As $M_{c_{is}}$ levels drop, $U_{c_{is}}$ is found to slightly increase. The measured convection velocity using two-time–two-point correlations provides lower values than the isentropic estimation which is consistent with the fluidic reattachment process. However, as M_r drops, U_c quickly increases until it nearly reaches the isentropic value of $0.8U_\infty$ at $x/L_R = 3$.

Concerning the structure of the wake, experimental visualizations (Bourdon & Dutton 1999, 2000) have demonstrated the highly convoluted nature of the developing wake. To compare the experimental observations to the present simulation, the streamwise evolution of the wake is depicted in figure 29 for five different stations after the rear stagnation point.

On moving downstream, the number of azimuthal structures decreases in accordance with the experimental observations. A high-mixing region can be seen where the fluid is engulfed inside the wake thanks to the three-dimensionality of the flow. As the wake develops, a lobbed structure can be seen for the farther stations in addition to the large-scale hairpin eddies educed by an iso-surface of the Q criterion depicted in figure 4.

According to the previous findings, the turbulence field organization is investigated through the use of the instantaneous shear stress angle Ψ in the developing wake. Figure 30 depicts the PDF of Ψ for two different streamwise stations in the wake.

Both stations exhibit identical trends. On the wake axis, no peak is observed in the PDF of Ψ. However, a preferential Ψ value exists at the outer wake boundary. For the radial location investigated here ($r/R \sim 0.37$), an angle of 30° is observed involving an organization of the turbulence field through the existence of the large-scale vortices.

7.3. *Spectral analysis*

The occurrence of large-scale structures in the far field of bi-dimensional supersonic base flows has been highlighted in some experiments by Motallebi & Norbury (1981) and by Gai, Hughes & Perry (2002) who have reported the existence of a shedding-type phenomenon in the far field of the wake similar to the one observed in the subsonic regime.

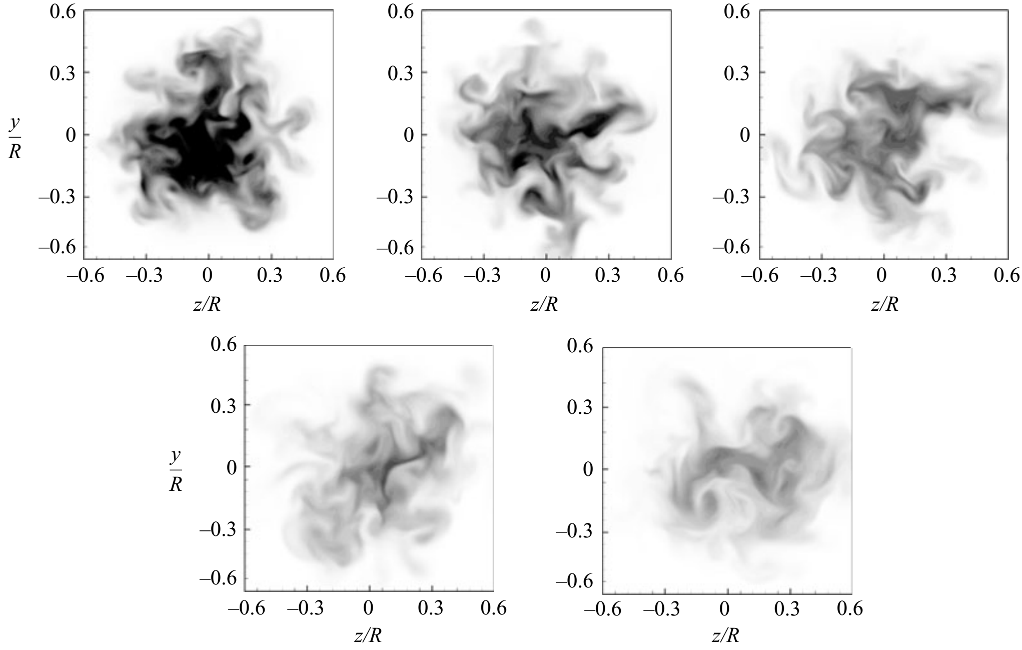

FIGURE 29. Instantaneous end views of iso-contours of Mach number in the wake ($1.2 < x/L_R < 2$). Each picture is offset by $0.2 \times x/L_R$ from top left to bottom right.

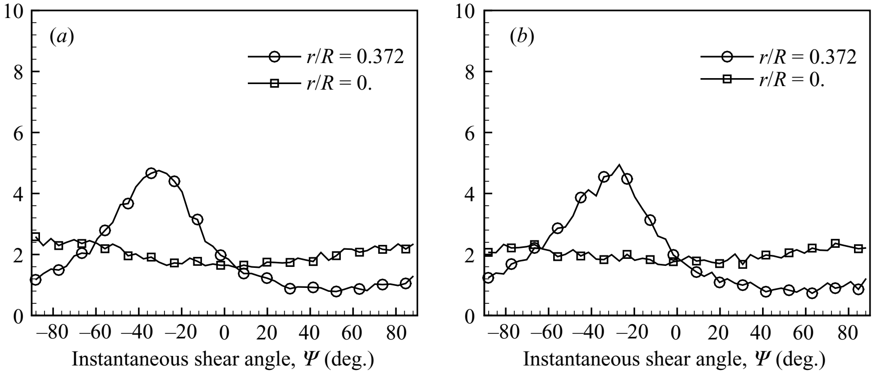

FIGURE 30. PDF of instantaneous shear angle Ψ on the wake axis at respectively (a) $x/R \sim 3.38$ and (b) $x/R \sim 4.02$.

The existence of such a phenomenon in the present flow has been shown by investigating the spectral content for a ring of sensors located in the outer part of the wake. As previously done by Fuchs *et al.* (1979) behind a circular disk, a mode decomposition in the azimuthal direction has been performed.

Figure 31 depicts the spectra of the four first azimuthal modes. A contribution of the first mode ($m = 1$), also called the helical mode, is found for a frequency close to 2400 Hz. This frequency, scaled with the diameter of the trailing edge, leads to a Strouhal number equal to $St_D \sim 0.256$. This value agrees well with the vortex shedding behind bluff bodies observed in supersonic flows (Motallebi & Norbury 1981, Gai *et al.* 2002). Moreover, the helical mode is known to be responsible for

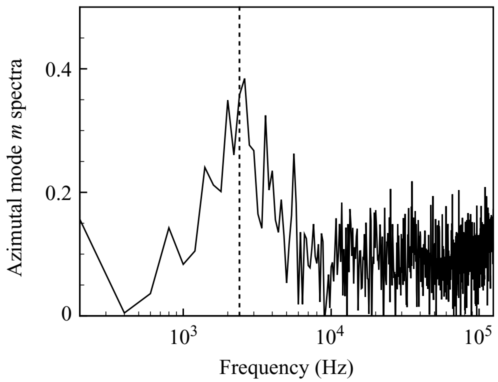

FIGURE 31. Azimuthal modal decomposition spectra of longitudinal velocity fluctuations at $x/R \sim 5.3$ and $r/R \sim 0.37$ for 47 azimuthal sensors ($m = 1$).

the shedding-type events in axisymmetric subsonic wakes. However, note that these structures appear less coherent than in the incompressible regime as reported by Gai (2002).

The present section is devoted to the study of the transition region between the axisymmetric shear layer and the fully developed wake. The compressibility effects are found to rapidly decrease with respect to the relative Mach number evolution. This is confirmed by measurements of U_c which increases after the rear stagnation point until reaching the isentropic model predictions. Finally, a modal decomposition has revealed the existence of a periodic phenomenon at $St_D \sim 0.256$ for the helical mode ($m = 1$). Such results corroborate previous findings reported for supersonic flows past planar trailing edge. The next section will discuss the unsteady features of the recirculating flow.

8. The recirculation zone

8.1. *Backflow analysis*

The recirculating bubble has been called a 'dead water' region. However, the visualizations of the flow field depict an area exhibiting deep unsteady features in the low-frequency as well as in the high-frequency regimes. As a result, the existence of convective phenomena inside the recirculating area has been tracked with the use of frequency–wavenumber spectra and the results, obtained with the use of all the available sensors in the backflow (44 sensors), are presented in figure 32.

Both the axial and radial velocity spectra exhibit a downstream velocity convection corresponding to the backflow disturbances; the velocity appears to be equal to approximately 230 m s^{-1} for both spectra but lower convective speeds exist as U_c varies depending on the location in the reverse flow (similarly to the mixing layer where frequency–wavemunber spectra exhibit only one convective velocity unlike the two-point–two-time correlations which reveal a varying speed of the eddies along the layer). Moreover, an additional feature appears in the radial (and transverse) fluctuation spectrum for the overall wavenumber range denoting a global motion of the backflow. This particular behaviour occurs for frequencies in the range of 1100–1200 Hz. Concerning the pressure evolution spectra for the both first (figure 32*c*) and the second half of the sensors (figure 32*d*) have been investigated. Both upstream and downstream travelling pressure waves are observed in (*c*) whereas only the

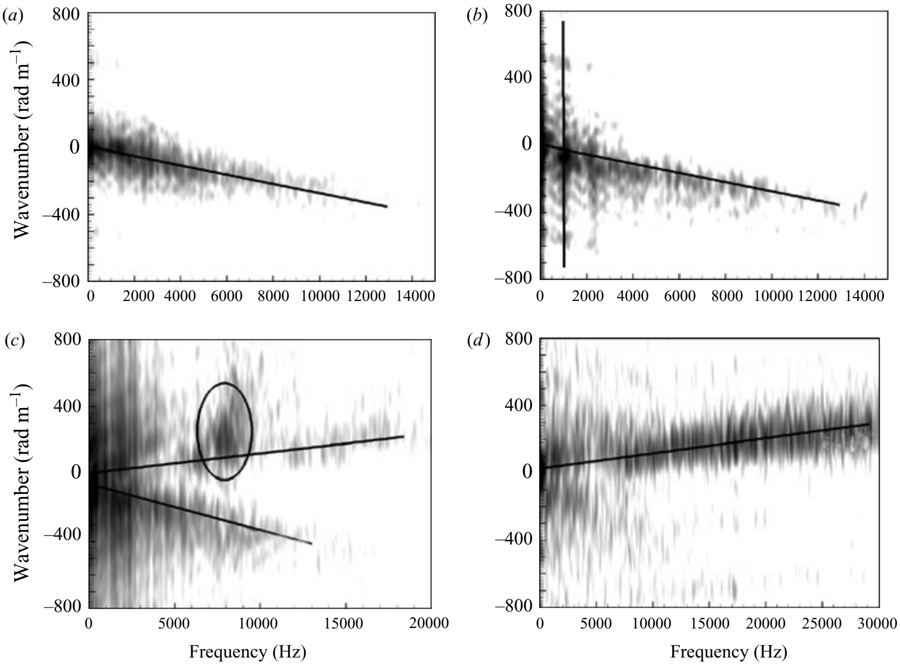

FIGURE 32. Frequency-wavenumber spectra of (*a*) the longitudinal velocity, (*b*) and the radial velocity; and (*c*) of the pressure first half of the recirculation area and (*d*) in the second half.

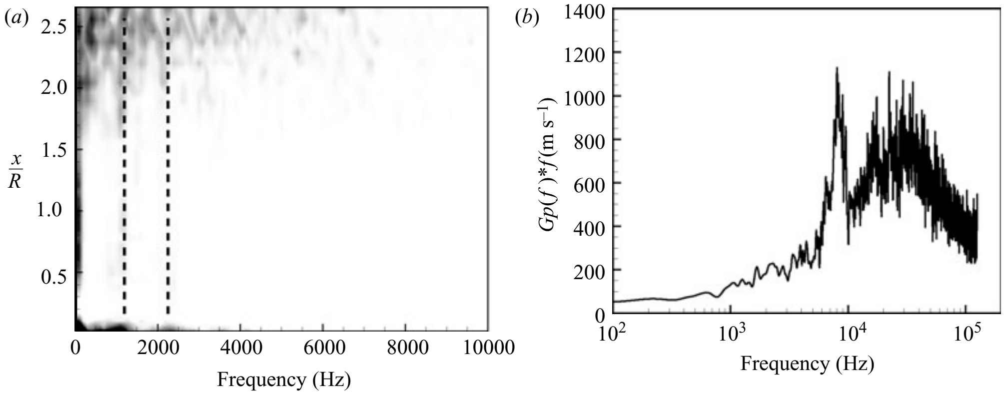

FIGURE 33. (*a*) PSD surface of radial velocity fluctuations along the axis in the reverse flow and (*b*) PSD of pressure fluctuations for the maximum backflow velocity location.

downstream travelling part is clearly visible in (*d*). The second half of the backflow is dominated by the pressure waves emanating from the vortices of the mixing layer which explains the downstream velocity. The upstream waves in (*c*) represent the pressure disturbances of the reverse flow, as encountered for the velocity spectra. A particular phenomena can be observed in figure 32(*c*) where a spot is clearly visible in the spectrum around 8000 Hz.

To assess the frequency content of the reverse flow, the spectra of the whole series of sensors located on the centreline have also been investigated by the use of PSD surfaces. An example is plotted in figure 33(*a*) which addresses the frequency content of

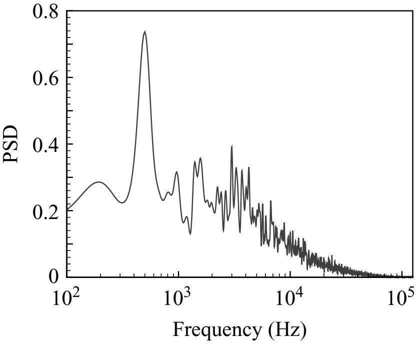

FIGURE 34. PSD of longitudinal velocity fluctuations on the wake axis at $x/R \sim 2.87$

the radial velocity fluctuations. Despite the broadband fluctuating content around the rear stagnation point, two lower frequencies can clearly be observed along the whole reverse flow at respectively 1250 Hz and 2250 Hz. The first contribution is similar to that previously observed in the frequency–wavenumber spectra of the radial velocity (see figure 32*b*). Although not shown here, such a contribution is also observed in the pressure spectra at the base, with maximum amplitude encountered around $x/R \sim 0.5$. This is consistent with a global motion of the whole reverse velocity axis around its mean position for both the radial and transverse components and confirms the previous observation made during the study of the frequency–wavenumber spectra. Such further evidence for this is found when looking at the movies which depict a slow oscillation of the reverse flow in the $(x,\ y)$-plane. Moreover, this motion would be consistent with the displacement of the instantaneous recirculation core centroid position observed in the experiment by Bourdon & Dutton (2000) and would constitute a characteristic feature of separated flows past an axisymmetric blunt trailing edge (opposite to backward-facing step configurations where any motion of the reverse flow would be prevented by the solid boundary).

The pressure spectra have also been investigated. However, the complex system of pressure waves inside the recirculation bubble made them quite difficult to discuss. Pressure waves emanating from the lower side of the vortices in the mixing layer travel downstream in the subsonic part of the flow whereas, at the same time, pressure disturbances originating from the reverse flow travel upstream. Despite such a complexity in the travelling wave pattern, a clear peak is observed on the pressure spectra for a position corresponding to approximately the location of the maximum backflow velocity (in a time-averaged sense). This behaviour is depicted in figure 33(*b*) where it is obvious that a strong phenomenon, having a purely acoustic nature with respect to the velocity fluctuations spectra, occurs at 8 kHz. Moreover, cross-correlations of the pressure signals in the vicinity of the maximum reverse flow underline the existence of a convective motion with velocity nearly equal to the local speed of sound. This may be the signature of a resonant mechanism of the pressure waves enclosed inside the sonic surface.

In addition to the motion of the reverse flow, some evidence of a pulsing motion can be educed by plotting streamwise velocity fluctuation spectra just ahead and downstream of the time-averaged stagnation point. An example is plotted in figure 34 where a location downstream of the rear stagnation point is considered.

The PSD spectrum reveals the existence of a sharp peak at approximately 500 Hz ($St_D \sim 0.053$ or $St_L \sim 0.072$). This frequency, too low to represent the occurrence of convected large-scale structures, may be the signature of a global flow behaviour. Although not shown here, a cross-spectra analysis (between the sensor located nearest to the base and one located at the stagnation point) exhibits coherence level above the onset of coherence required by the method, which corroborates the assumption about large-scale unsteadiness. The existence of such a similar frequency in both experimental (Janssen & Dutton 2004) and numerical pressure spectra at the base centre is further evidence of a growing/contracting motion of the whole recirculating flow. In the other part of the flow, the spectral signature of this motion may be lost among stronger fluctuating contributions. It is interesting to note that Shvets (1979) has also observed a low-frequency component in the vicinity of the rear stagnation point in the near wake of a cone in the supersonic regime, consistent with his experimental visualizations of a global motion of the whole separated flow behind the base. Evidence of the existence of such a low-frequency contribution exists in previous work dealing with separated flow behind an axisymmetric trailing edge in the subsonic regime. Thus, both Mabey (1972) and Deprés (2003) have respectively reported characteristic Strouhal numbers St_D equal to 0.06 and 0.068 at the base centre for axisymmetric base flows.

8.2. *Feedback mechanism*

As previously mentioned, the recirculating flow area exhibits a very complex physics when focusing on its unsteady properties and may be responsible for the existence of a feedback mechanism triggering the shear layer instability and the self-sustained oscillations observed in the near wake. Two mechanisms are known to be involved in such a feedback loop.

The first one concerns oscillations due to the impingement of pressure waves on a solid surface, thus leading to a forcing of the shear layer instability (see the review by Rockwell 1983). Such a mechanism may exist in the present flow as the pressure waves radiating from the coherent vortices on their lower side and those emanating from the reverse flow can be trapped in the subsonic area and can lead to a resonant phenomenon inside the closed sonic surface.

Another mechanism which may be responsible for the appearance of self-sustained oscillations is the existence of an absolute instability (see Huerre & Monkewitz (1985) for a detailed analysis of convective/absolute instabilities). Monkewitz (1988) has highlighted the absolutely unstable nature of the first helical mode in the near wake of incompressible axisymmetric bluff bodies for a Reynolds number where self-sustained oscillations are observed. The stability properties of the flow depend upon the mean local velocity profile. Sevilla & Martinez-Bazan (2004) have demonstrated that modifying the reverse flow component of the velocity profile can lead to a shift from an absolute to a convective instability of the recirculating flow and thus suppresses the vortex shedding occurring in the near wake. The concept of absolute instability has also recently been applied to incompressible backward-facing step flows by Wee *et al.* (2004) and to a flow behind a fence by Hudy, Naguib & Humphreys (2003) and Naguib & Hudy (2003). Wee *et al.* (2004) perform a linear stability analysis to highlight the existence of an absolute instability in the middle of the reverse flow area with $St_h \sim 0.067$ (h is the step height). Hudy *et al.* (2003) have also observed the existence of an absolute instability as a source for upstream and downstream travelling pressure waves in the recirculating flow. As the absolute nature of the flow mainly depends on the time-averaged velocity profile, such an instability can exist in the present flow despite its compressible nature, in accordance with the self-sustained oscillations observed in the developing wake. Very recently, Sandberg & Fasel (2006*b*) have investigated the transitional base flow at $M_\infty = 2.46$ and have demonstrated the existence of an absolute instability for the axisymmetric mode at moderate Reynolds number. This finding makes it highly likely that such an instability exists in the present flow and could be related to the large-scale unsteadiness discussed in the previous section.

Finally, the existence of a secondary vortex structure in the vicinity of the base corner could play a significant role in the forcing of the shear layer. As in the simulation of Larchevêque *et al.* (2004) concerning the compressible flow past a cavity, a secondary vortex exists in both the time-averaged and instantaneous flow fields. An animation focusing on this particular part of the flow reveals that the vortex dynamics participates to a certain extent to the generation of large-scale structures downstream in the mixing layer during a burst-like phenomenon.

9. Conclusions

A numerical simulation has been carried out of a compressible axisymmetric shear layer for a Reynolds number near 2.9×10^6. The supersonic free-stream Mach number before separation involves complex behaviour of the annular mixing layer with the appearance of several characteristic features. Each part of the flow has been successively discussed in the light of both time-averaged and unsteady data. The development of the mixing layer has underlined the strong growth rate of the shear layer ahead of recompression.

The peak Reynolds stresses increase until the onset of recompression. On entering the adverse pressure gradient, the turbulent stresses immediately react to the extra strain rate, in contrast to its incompressible counterpart. Despite the domination of the axial velocity fluctuations, the anisotropy decreases along the shear layer until a constant value of 1.25 is reached, denoting strong changes in the turbulence field organization. Correlation functions have been used to demonstrate the failure of the isentropic theory to properly predict the convection velocity of the vortices in the axisymmetric mixing layer which corroborates previous findings dealing with canonical planar compressible cases. In the present case, the fast mode dominates due to supersonic convective Mach numbers levels. The pressure gradient then leads to a deceleration of the eddies.

The lateral streamline convergence and the bulk compression involve a complex shock pattern in which the foot shock appears to be constituted by shocks emanating from the upper side of the vortices. Once the fluidic reattachement process is achieved, the compressibility of the flow is quickly damped allowing a recovery of the incompressible wake behaviour farther downstream. The use of numerous sensors has allowed the characteristics frequencies of the flow to be found, which was not possible during the experiment. A wide range of time scales has been highlighted, from the instability process behind the base to the existence of a global motion of the separated flow field at very low frequency denoting the very complex unsteady features of such flows and the difficulties of capturing the whole physics. Thus, further evidence of the existence of a flapping motion has been found and the oscillation of the reverse flow has been underlined. Finally, an even lower frequency, which may be due to the motion of the rear stagnation point, has been found.

The authors are greatly indebted to Professors J.C. Dutton, P. Cannon and J. Forsythe for providing the experimental data. This study is partly funded by Giat Industries within the framework of ONERA/Giat Industries cooperation. R. Cayzac is warmly acknowledged for very stimulating discussions. The authors thank

J. Dandois for fruitful discussions about separated/reattaching flows unsteadiness behind backward-facing steps.

REFERENCES

Adams, N. A. 2000 Direct simulation of the turbulent boundary layer along a compression ramp at $M = 3$ and $Re_\theta = 1685$. *J. Fluid Mech.* **420**, 47–83.

Barre, S., Quine, C. & Dussauge, J. P. 1994 Compressibility effects on the structure of supersonic mixing layers: experimental results. *J. Fluid Mech.* **259**, 47–78.

Baurle, R. A., Tam, C.-J., Edwards, J. R. & Hassan, H. A. 2003 Hybrid simulation approach for cavity flows: blending, algorithm, and boundary treatment issues. *AIAA J.* **41**, 1463–1480.

Bell, J. H. & Mehta, R. D. 1990 Development of a two-stream mixing layer from tripped and untripped boundary layers. *AIAA J.* **28**, 2034–2042.

Bogdanoff, D. W. 1983 Compressibility effects in turbulent shear layers. *AIAA J.* **21**, 926–927.

Bourdon, C. J. & Dutton, J. C. 1999 Planar visualizations of large-scale turbulent structures in axisymmetric supersonic flow. *AIAA J.* **11**, 201–213.

Bourdon, C. J. & Dutton, J. C. 2000 Shear layer flapping and interface convolution in a separated supersonic flow. *AIAA J.* **38**, 1907–1915.

Bourdon, C. J. & Dutton, J. C. 2001 Effects of boattailing on the turbulence structure of a compressible base flow. *J. Spacecraft Rockets* **38**, 534–541.

Bradshaw, P. 1974 The effect of mean compression or dilatation on the turbulence structure for supersonic boundary layers. *J. Fluid Mech.* **63**, 449–464.

Breidenthal, R. 1990 The sonic eddy – a model for compressible turbulence. *AIAA Paper* 90-0495.

Breuer, M., Jocivic, N. & Mazaev, K. 2003 Comparison of DES, RANS and LES for the separated flow around a flate plate at high incidence. *Intl. J. Numer. Meth. Fluids* **41**, 357–388.

Bunyajitradulya, A. & Papamoschou, D. 1994 Acetone PLIF imaging of turbulent shear-layer structure at high convective Mach number. *AIAA Paper* 94-0617.

Cannon, P. M., Elliott, G. S. & Dutton, J. C. 2005 Time-series axisymmetric base-pressure measurements with simultaneous near-wake visualizations. *AIAA Paper* 2005-5285.

Chandrsuda, C. & Bradshaw, P. 1981 Turbulence structure of a reattaching mixing layer. *J. Fluid Mech.* **110**, 171–194.

Clemens, N. T. & Mungal, M. G. 1995 Large-scale structure and entrainment in the supersonic mixing layer. *J. Fluid Mech.* **284**, 171–216.

Clemens, N. T., Petullo, S. P. & Dolling, D. S. 1996 Large-scale structure evolution in supersonic interacting shear layers. *AIAA J.* **34**, 2062–2070.

Dandois, J., Garnier, E. & Sagaut, P. 2007 Numerical simulation of active separation control by a synthetic jet. *J. Fluid Mech.* **574**, 25–58.

Deck, S., Garnier, E. & Guillen, P. 2002 Turbulence modelling applied to space launcher configurations. *J. Turbulence* **3**, 1–21.

Deck, S., Duveau, P., d'Espiney, P. & Guillen, P. 2002 Development and application of Spalart Allmaras one equation turbulence model to three-dimensional supersonic complex configurations. *Aerospace Sci. Tech.* **6**, 171–183.

Deck, S. 2005*a* Numerical simulation of transonic buffet over a supercritical airfoil. *AIAA J.* **43**, 1556–1566.

Deck, S. 2005*b* Zonal-detached eddy simulation of the flow around a high-lift configuration. *AIAA J.* **43**, 2372–2384.

Deck, S. & Thorigny, P. 2007 Unsteadiness of an axisymmetric separating-reattaching flow. *Phys. Fluids* **19**, 065103.

Demetriades, A. 1968 Turbulent front structure of an axisymmetric compressible wake. *J. Fluid Mech.* **34**, 465–480.

Demetriades, A. 1976 Turbulence correlations in a compressible wake. *J. Fluid Mech.* **74**, 251–267.

Deprés, D. 2003 Analyse physique et modélisation des instationnarités dans les écoulements d'arrière-corps transsoniques. PhD thesis, University of Aix-Marseille.

Dolling, S. & Murphy, M. T. 1983 Unsteadiness of the separation shock wave structure in a supersonic ramp flowfield. *AIAA J.* **12**, 1628–1634.

DOLLING, S. 2001 Fifty years of shock-wave/boundary-layer interaction research: what next? *AIAA J.* **39**, 1517–1531.

ELLIOT, G. S., SAMIMY, M. & ARNETTE, S. A. 1995 The characteristics and evolution of large-scale structures in compressible mixing-layers. *Phys. Fluids* **7**, 864.

ERLEBACHER, G., HUSSAINI, M. Y., SPEZIALE, C. G. & ZANG, T. A. 1992 Toward the large-eddy simulation of compressible turbulent flows. *J. Fluid Mech.* **238**, 155–185.

FORSYTHE, J. R., HOFFMAN, K. A., CUMMINGS, R. M. & SQUIRES, K. D. 2002 Detached-eddy simulation with compressibility corrections applied to a supersonic axisymmetric base flow. *J. Fluids Engng. Trans. ASME*: **124**, 911–923.

FOURGUETTE, D. C., MUNGAL, M. G. & DIBBLE, R. W. 1991 Time evolution of the shear layer of a supersonic axisymmetric jet. *AIAA J.* **29**, 1123–1130.

FREUND, J. B., LELE, S. K. & MOIN, P. 2000 Compressibility effects in a turbulent annular mixing layer. Part 1. Turbulence and growth rate. *J. Fluid Mech.* **421**, 229–267.

FRIEDRICH, R. & ARNAL, M. 1990 Analysing turbulent backward-facing step flow with the lowpass-filtered Navier-Stokes equations. *J. Wind Engng Ind. Aerodyn.* **35**, 101–128.

FUCHS, H. V., MERCKER, E. & MICHEL, U. 1979 Large-scale coherent structures in the wake of axisymmetric bodies. *J. Fluid Mech.* **93**, 185–207.

FUREBY, C., NILSSON, Y. & ANDERSSON, K. 1999 Large-eddy simulation of supersonic base flow. *AIAA Paper* 99-0426.

GAI, S. L., HUGHES, D. P. & PERRY, M. S. 2002 Large-scale structures and growth of a flat plate compressible wake. *AIAA J.* **40**, 1164–1169.

GAVIGLIO, J., DUSSAUGE, J.-P., DEBIEVE, J.-F. & FAVRE, A. 1977 Behavior of a turbulent flow, strongly out of equilibrium, at supersonic speeds. *Phys. Fluids* **20**, 179–192.

GOEBEL, S. G. & DUTTON, J. G. 1990 Experimental study of compressible turbulent mixing layers. *AIAA J.* **29**, 538–546.

GRUBER, M. R., MESSERSMITH, N. L. & DUTTON, J. G. 1993 Three-dimensional velocity field in a compressible mixing layer. *AIAA J.* **31**, 2061–2067.

HARSHA, P. T. & LEE, S. C. 1970 Correlation between turbulent shear stress and turbulent kinetic energy. *AIAA J.* **8**, 1508.

HERRIN, J. L. & DUTTON, J. C. 1994*a* Supersonic base flow experiments in the near wake of a cylindrical afterbody. *AIAA J.* **32**, 77–83.

HERRIN, J. L. & DUTTON, J. C. 1994*b* Supersonic near-wake afterbody boattailing effects on axisymmetric bodies. *J. Spacecraft Rockets* **31**, 1021–1028.

HERRIN, J. L. & DUTTON, J. C. 1995 Effect of a rapid expansion on the development of compressible free shear layers. *Phys. Fluids* **7**, 159–171.

HERRIN, J. L. & DUTTON, J. C. 1997 The turbulence structure of a reattaching axisymmetric compressible free shear layer. *Phys. Fluids* **9**, 3502–3512.

HUDY, L. M., NAGUIB, A. M. & HUMPHREYS JR, W. M. 2003 Wall-presure-array measurements beneath a separating/reattaching flow region. *Phys. Fluids* **15**, 706–717.

HUERRE, P. & MONKEWITZ, P. A. 1985 Absolute and convective instabilities in free shear layers. *J. Fluid Mech.* **159**, 151–168.

JACKSON, T. L. & GROSCH, C. E. 1989 Inviscid spatial stability of a compressible mixing layer. *J. Fluid Mech.* **208**, 609–637.

JANSSEN, J. R. & DUTTON, J. C. 2004 Time-series analysis of supersonic basepressure fluctuations. *AIAA J.* **43**, 605–613.

JEONG, J. & HUSSAIN, F. 1995 On the identification of a vortex. *J. Fluid Mech.* **285**, 69–94.

JOVIC, S. 1996 An experimental study of a separated/reattached flow behind a backward-facing step. $Re_H = 37{,}000$. *NASA Tech. Mem.* 110384.

KAWAI, S. & FUJII, K. 2005 Computational study of supersonic base flow using hybrid turbulence methodology. *AIAA J.* **43**, 1265–1275.

LARCHEVÊQUE, L., SAGAUT, P., MARY, I., LABBÉ, O. & COMTE, P. 2003 Large-eddy simulation of a compressible flow past a deep cavity. *Phys. Fluids* **15**, 193–210.

LARCHEVÊQUE, L., SAGAUT, P., LÊ, T.H. & COMTE, P. 2004 Large-eddy simulation of a compressible flow in a three-dimensional open cavity at high Reynolds number. *J. Fluid Mech.* **516**, 265–301.

MAHADEVAN, R. & LOTH, E. 1994 High-speed cinematography of compressible mixing layers. *Exps. Fluids* **17**, 179.

Martens, S., Kimzie, K. W. & McLaughlin, D. K. 1994 Wave structure of coherent instabilities in a planar shear layer. *AIAA Paper* 94-0822.

Mary, I. & Sagaut, P. 2002 Large-eddy simulation of a flow around an airfoil near stall. *AIAA J.* **40**, 1139–1145.

Mabey, D. G. 1972 Analysis and correlation of data on pressure fluctuations in separated flow. *J. Aircraft* **9**, 642–645.

Messersmith, N. L. & Dutton, J. C. 1996 Characteristic features of large structures in compressible mixing layers. *AIAA J.* **34**, 1814–1821.

Monkewitz, P. A. 1988 A note on vortex shedding from axisymmetric bluff bodies. *J. Fluid Mech.* **192**, 561–575.

Motallebi, F. & Norbury, J. F. 1981 The effect of base bleed on vortex shedding and base pressure in compressible flow. *J. Fluid Mech.* **110**, 272–292.

Naguib, A. M. & Hudy, L. M. 2003 Stationary and propagating low-frequency wall-pressure disturbances in a separating/reattaching flow. *AIAA Paper* 2003-1126.

Olsen, M. G. & Dutton, J. G. 2003 Planar velocity measurements in a weakly compressible mixing layer. *J. Fluid Mech.* **486**, 51–77.

Pantano, C. & Sarkar, S. 2002 A study of compressibility effects in the highspeed turbulent shear layer using direct simulation. *J. Fluid Mech.* **451**, 329–371.

Papamoschou, D. & Roshko, A. 1988 The compressible turbulent shear layer: an experimental study. *J. Fluid Mech.* **197**, 453–477.

Papamoschou, D. 1990 Communication paths in the compressible shear layer. *AIAA Paper* 90-0155.

Papamoschou, D. 1991 Structure of the compressible turbulent shear layer. *AIAA J.* **29**, 680.

Papamoschou, D. & Bunyajitradulya, A. 1995 Double-exposure PLIF imaging of compressible shear layers. *AIAA Paper* 95-0531.

Papamoschou, D. & Bunyajitradulya, A. 1997 Evolution of large eddies in compressible shear layers. *Phys. Fluids* **9**, 756.

Péchier, M., Guillen, P. & Cayzac, R. 2001 Magnus effect over finned projectiles *J. Spacecraft Rockets* **38**, 542–549.

Poggie, J. & Smits, A. J. 1996 Large-scale coherent turbulence structures in a compressible mixing layer flow. *AIAA Paper* 96-0440.

Poggie, J. & Smits, A. J. 2001 Shock unsteadiness in a reattaching shear layer. *J. Fluid Mech.* **429**, 155–185.

Roberts, J. B. 1973 Coherence measurements in an axisymmetric wake. *AIAA J.* **11**, 1569–1571.

Rockwell, D. 1983 Oscillations of impinging shear layers. *AIAA J.* **21**, 645–664.

Sagaut, P., Deck, S. & Terracol, M. 2006 *Multiscale and Multiresolution Approaches in Turbulence.* Imperial College Press, London, UK.

Samimy, M., Petrie, H. L. & Addy, A. L. 1986 A study of compressible turbulent reattaching free shear layers. *AIAA J.* **24**, 261–267.

Samimy, M. & Elliot, G. S. 1990 Effects of compressibility on the characteristics of free shear flows. *AIAA J.* **28**, 439–445.

Sandbberg, R. D. & Fasel, H. F. 2006*a* Direct numerical simulation of transitional supersonic base flows. *AIAA J.* **44**, 848–858.

Sandberg, R. D. & Fasel, H. F. 2006*b* Numerical investigation of transitional supersonic axisymmetric wakes. *J. Fluid Mech.* **563**, 1–41.

Sandham, N. D. & Reynolds, W. C. 1989 Compressible mixing layer: linear theory and direct simulation. *AIAA J.* **28**, 618–624.

Sandham, N. D. & Reynolds, W. C. 1991 Threedimensional simulations of large eddies in the compressible mixing layer. *J. Fluid Mech.* **224**, 133–158.

Sarkar, S. 1995 The stabilizing effect of compressibility in turbulent shear flow. *J. Fluid Mech.* **282**, 163–186.

Sevilla, A. & Martinez-Bazan, C. 2004 Vortex shedding in high Reynolds number axisymmetric bluff-body wakes : Local linear instability and global bleed control. *Phys. Fluids* **16**, 3460–3469.

Shur, M., Spalart, P., Strelets, M. & Travin, A. 1999 Detached-eddy simulation of an airfoil at high angle of attack. *4th Intl. Symp. Engineering Turbulence Modelling and Measurements*, pp. 669–678. Elsevier.

Shvets, A. I. 1979 Base pressure fluctuations. *Fluid Dyn.* **14**, 394–401.

Simon, F., Deck, S., Guillen, P. & Sagaut, P. 2006 RANS/LES simulations of supersonic base flow. *AIAA J.* **44**, 2578–2590.

Simon, F., Deck, S., Guillen, P., Cayzac, R. & Merlen, A. 2007 Zonal-detached-eddy simulation of projectiles in the subsonic and transonic regimes. *AIAA J.* **45**, 1606–1619.

Simone, A., Coleman, G. N. & Cambon, C. 1997 The effect of compressibility on turbulent shear flow: a rapiddistorsiontheory and directnumericalsimulation study. *J. Fluid Mech.* **330**, 307–338.

Smith, K. M. & Dutton, J. C. 1996 Investigation of large-scale structures in supersonic planar base flows. *AIAA J.* **34**, 1146–1152.

Smith, K. M. & Dutton, J. C. 1999 Evolution and convection of large-scale structures in supersonic reattaching shear flows. *Phys. Fluids* **11**, 2127–2138.

Smith, K. M. & Dutton, J. C. 2001 The effects of expansion strength on large-scale structures in compressible free shear layers. *Phys. Fluids* **13**, 2076–2086.

Spalart, P. R. & Allmaras, S. R. 1992 A one equation turbulence model for aerodynamic flows. *AIAA Paper* 92-0439.

Spalart, P. R. & Allmaras, S. R. 1994 A one equation turbulence model for aerodynamic flows. *La Recherche Aérospatiale*, 5–21.

Spalart, P., Jou, W. H., Strelets, M. & Allmaras, S. R. 1997 Comments on the feasibility of LES for wings and on a hybrid RANS/LES approach. *In Proc. 1st AFSOR Int. Conf. on DNS/LES, Ruston.*

Spalart, P. R. 2001 Young-person's guide to detached-eddy simulation grids. *NASA/CR-2001*-211032.

Spalart, P. R., Deck, S., Shur, M. L., Squires, K. D., Strelets, M. K. & Travin, A. 2006 A new version of detached-eddy simulation, resistant to ambiguous grid densities. *Theor. Comput. Fluid Dyn.* **20**, 181–195.

Thurow, B., Samimy, M. & Lempert, W. 2003 Compressibility effects on turbulence structures of axisymmetric mixing layers. *Phys. Fluids* **15 (6)**, 1755–1765.

Urban, W. D. & Mungal, M. G. 2001 Planar velocity measurements in compresible mixing layers *J. Fluid Mech.* **431**, 189–222.

Vreman, A. W., Sandham, N. D. & Luo, K. H. 1996 Compressible mixing layer growth rate and turbulence characteristics. *J. Fluid Mech.* **320**, 235–258.

Vreman, B., Geurts, B. & Kuerten, H. 1997 Large-eddy simulation of the turbulent mixing layer. *J. Fluid Mech.* **339**, 357–390.

Wee, D., Yi, T., Annaswamy, A. & Ghoniem, A. F. 2004 Self-sustained oscillations and vortex shedding in backward-facing step flows: Simulation and linear instability analysis. *Phys. Fluids* **16**, 3361–3373.

Wu, P. P. & Miles, R. B. 2001 Megahertz visualization of compression-corner shock structures. *AIAA J.* **39**, 1542–1546.